J. Fluid Mech. (2019), *vol.* 859, *pp.* 586–612. © Cambridge University Press 2018
doi:10.1017/jfm.2018.799

Locomotion of a single-flagellated bacterium

Yunyoung Park[1], **Yongsam Kim**[1,†] **and Sookkyung Lim**[2]

[1]Department of Mathematics, Chung-Ang University, Dongjakgu, Heukseokdong, Seoul 06974, Republic of Korea

[2]Department of Mathematical Sciences, University of Cincinnati, 4199 French Hall West, Cincinnati, OH 45221, USA

(Received 25 February 2018; revised 29 September 2018; accepted 3 October 2018; first published online 21 November 2018)

Single-flagellated bacteria propel themselves by rotating a flagellar motor, translating rotation to the filament through a compliant hook and subsequently driving the rotation of the flagellum. The flagellar motor alternates the direction of rotation between counterclockwise and clockwise, and this leads to the forward and backward directed swimming. Such bacteria can change the course of swimming as the hook experiences its buckling caused by the change of bending rigidity. In this paper, we present a comprehensive model of a monotrichous bacterium as a free swimmer in a viscous fluid. We describe a cell body as a rigid body using the penalty method and a flagellum as an elastic rod using Kirchhoff rod theory. The hydrodynamic interaction of the bacterium is described by the regularized Stokes formulation. Our model of a single-flagellated micro-organism is able to mimic a swimming pattern that is well matched with the experimental observation. Furthermore, we find the critical thresholds of the rotational frequency of the motor and the bending modulus of the hook for the buckling instability, and investigate the dependence of the buckling angle and the reorientation of the swimming cell after buckling on the physical and geometrical parameters of the model.

Key words: micro-organism dynamics, swimming/flying

1. Introduction

Swimming bacteria with flagella are self-propelled micro-swimmers in nature, and the swimming strategies of such bacteria vary depending on the number and the position of flagella on the cell body. In bacterial flagella-based propulsion, the major driving force, commonly observed by many flagellated bacteria, comes from a rotary motor which is embedded in the cell body and is connected to the flagellar filament via a universal joint called a hook (Berg & Anderson 1973; Ramia, Tullock & Phan-Thien 1993; Purcell 1997; McCarter 2001; Berg 2003; Sen, Nandy & Ghosh 2004; Chattopadhyay & Wu 2009; Lauga & Powers 2009; Stocker 2011; Lauga 2016).

Of the flagellated micro-organisms, monotrichous bacteria such as *Vibrio alginolyticus* have a single left-handed helical flagellum protruding from one end of the major axis

† Email address for correspondence: kimy@cau.ac.kr

https://doi.org/10.1017/jfm.2018.799 Published online by Cambridge University Press

of the rod-shaped cell body. The flagellar motor spins either counterclockwise (CCW) or clockwise (CW), and the rotation of the motor is transmitted by a short, straight hook to the flagellar filament, resulting in directed forward or backward swimming (Homma *et al.* 1996; Furuno *et al.* 1997; Magariyama *et al.* 2001; Chattopadhyay & Wu 2009; Xie *et al.* 2010; Son, Guasto & Stocher 2013). This marine bacterium changes its swimming direction by exploiting a finely tuned buckling instability caused by the change of the loaded state of the hook. It is known that the hook is much more flexible than the flagellar filament, differing by several orders of magnitude in bending rigidity, and its length is substantially shorter than that of the filament, yielding a length ratio of approximately 50 (Flynn & Ma 2004; Sen *et al.* 2004; Son *et al.* 2013).

The monotrichous bacterium swims backward by turning the motor CW while the hook is under tension. Then the motor reverses suddenly and the bacterium swims forward, which causes the hook to be in a compressed state. A dynamic stiffening of the hook (loaded state) during steady swimming has been observed through direct measurements (Son *et al.* 2013), and the hook becomes more flexible (relaxed state) on the reversal of the motor's rotational direction. The bending stiffness of the relaxed hook was measured to be 4–6 times smaller than that of the loaded hook. The reason for this stiffness change can be explained by the motor's torsional load (Block, Blair & Berg 1989, 1991); that is, when the motor reverses, the hook temporarily unwinds, losing the bending stiffness and becoming susceptible to buckling. The buckling of the hook is followed by the flicking of the bacterium, which eventually takes a straightforward run, possibly in a new direction. This 'run–reverse–flick' movement pattern is prevalent in motile monotrichous bacteria in the ocean (Stocker 2011).

Many analytical and numerical results have been presented for the dynamics of single-flagellated microorganisms (Taylor 1952; Hancock 1953; Chwang & Wu 1971; Higdon 1979; Phan-Thien, Tran-Cong & Ramia 1987; Ramia *et al.* 1993; Ishikawa *et al.* 2007; Hsu & Dillon 2009; Ishikawa 2009; Shum, Gaffney & Smith 2010; Shum & Gaffney 2012). In particular, Chwang & Wu (1971) used the resistive-force theory to analyse the helical movement of a microorganism with a spherical head, producing a propulsive force by propagating a helical wave along the filament. They investigated optimal conditions for swimming speed and the hydromechanical efficiency depending on the ratio of the head size and the filament length. Higdon (1979) and Phan-Thien *et al.* (1987) further analysed the optimal swimming motion by using the slender-body theory and the boundary element (BE) method, respectively, with a wide range of parameters for the geometrical properties of the cell body and flagellum. The BE method has also been widely used to investigate the swimming dynamics of a single-flagellated bacterium near a surface or in the vicinity of another organism (Ramia *et al.* 1993; Ishikawa *et al.* 2007; Ishikawa 2009). All previous models above, however, do not consider the mechanical properties of the filament and hook. Shum *et al.* (2010) and Shum & Gaffney (2012) first proposed a model organism that incorporates an elastic hook, while the filament is still rigid, to explore the function and effect of the hook on the motility of single-flagellated bacteria. The Kirchhoff rod theory combined with the BE method is used for their model dynamics. Recently Park *et al.* (2017) investigated the buckling instability of a single rotating flagellum composed of a flexible filament and hook, while the rotating motor is tethered in space. The dynamics of the flagellum is based on the Kirchhoff rod theory (Lim *et al.* 2008; Lim & Peskin 2012), and the hydrodynamic interaction of the flagellum is described by the regularized Stokes formulation (Olson, Lim & Cortez 2013). However, the model used in Park *et al.* (2017) does not include a moving cell body.

https://doi.org/10.1017/jfm.2018.799 Published online by Cambridge University Press

In this paper, we introduce a comprehensive model for a freely swimming monotrichous bacterium including a cell body and a flexible helical flagellum equipped with a motor connecting a hook to the cell body. Unlike most of the models in previous studies that consider a flagellum rigidly rotating about its axis, the filament and hook in our model are flexible so that they can bend and twist, as in Park *et al.* (2017). We rotate only the motor CW or CCW to generate the twist and thus a helical wave, which is transmitted along the flagellum to its free end, leads to the rotation of the helical filament. Furthermore, the interaction between the cell body and the flagellum is also taken into account. We use Kirchhoff rod theory to model the elastic helical flagellum (Lim *et al.* 2008; Park *et al.* 2017) and adopt the penalty idea (Kim & Peskin 2016) to describe the rigid-body dynamics of the cell body. The interaction between fluid and these immersed materials is represented by the regularized Stokes formulation (Olson *et al.* 2013).

We first validate our mathematical model of a monotrichous bacterium by comparing the swimming speed and power efficiency with those of Higdon (1979), who used the slender-body theory for Stokes flow and an image system for the cell body. We then investigate the dependence of the swimming speed and the rotation rate of the cell body on various physical parameters such as the rotational frequency of the motor, the fluid property and the geometrical shape of the cell body. Finally we find the critical thresholds of the rotational frequency of the motor and the bending modulus of the hook for the buckling instability and explore the dependence of the buckling angle and the change of the swimming direction after buckling on the physical and geometrical parameters of the model.

2. Mathematical model

The mathematical model of a single-flagellated bacterium consists of a cell body in the shape of an ellipsoid and a long helical flagellum as a propeller. The flagellum comprises three parts: a rotary motor, a helical filament and a flexible hook that bridges the motor and the filament. See figure 1 for a schematic diagram of our computational model. We describe the elastic flagellar filament and the hook using the Kirchhoff rod model, and use the penalty method to model the cell body as a rigid body. The hydrodynamic interaction between fluid and the bacterium is described by the regularized Stokes formulation (Olson *et al.* 2013).

2.1. *Filament and hook model: Kirchhoff rod theory*

In order to model the helical filament and a hook of bacteria, we adopt the Kirchhoff rod theory which uses a space curve $\boldsymbol{X}(s, t)$ to represent the centreline of the flagellum and an associated orthonormal triad $\boldsymbol{D}^i(s, t)$, $i = 1, 2, 3$, to measure the amount of bending and twisting of the flagellum: see the right-top panel of figure 1. Here, t is time and s is a Lagrangian coordinate along the rod with $0 \leqslant s \leqslant L_h + L_f$, where L_h and L_f are the lengths of the hook and the helical filament, respectively. The initial shape of the helical centreline $\boldsymbol{X}(s, 0)$ is described as follows (Higdon 1979):

$$\boldsymbol{X}(s, 0) = (r(s)\cos(\alpha s), r(s)\sin(\alpha s), s), \tag{2.1}$$

where α is the wavenumber and the helical radius $r(s)$ is a variable function defined as

$$r(s) = \begin{cases} 0 & 0 \leqslant s \leqslant L_h, \\ r_0(1 - \mathrm{e}^{-k_E(s-L_h)^2}) & L_h \leqslant s \leqslant L_h + L_f, \end{cases} \tag{2.2}$$

https://doi.org/10.1017/jfm.2018.799 Published online by Cambridge University Press

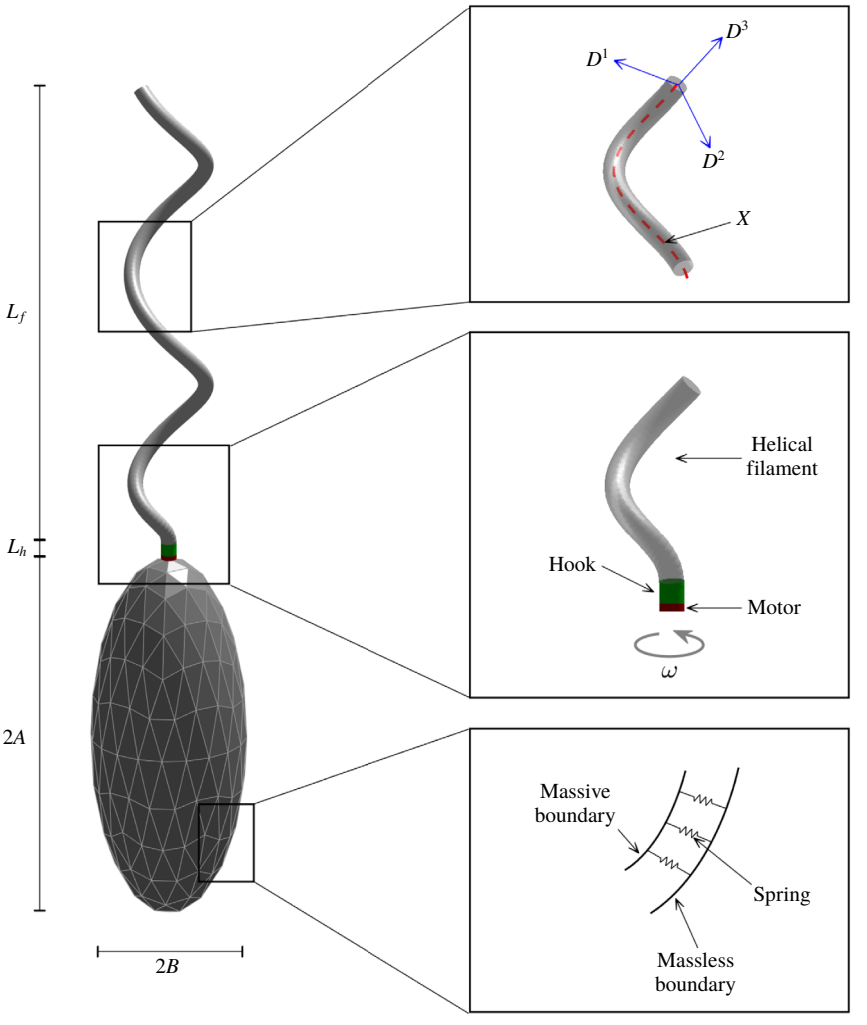


FIGURE 1. (Colour online) A schematic view of the computational model for a monotrichous bacterium with a left-handed helical flagellum and an ellipsoidal cell body. The right top panel shows the centreline of a helical rod $\boldsymbol{X}$ with an orthonormal triad $\{\boldsymbol{D}^1, \boldsymbol{D}^2, \boldsymbol{D}^3\}$. The helical flagellar filament is linked to a compliant hook, which is also linked to a rotary motor that is attached at the north pole of the ellipsoidal cell body (right middle). Massive and massless boundaries are linked together by a collection of very stiff springs with zero rest length (right bottom).

where k_E is a constant. The helical radius is 0 for the hook ($0 \leqslant s \leqslant L_h$) which is a straight rod, and then increases gradually to r_0 for the helical filament ($L_h \leqslant s \leqslant L_h + L_f$).

The vector $\boldsymbol{D}^3(s, 0)$ is initially defined as a unit tangent vector to the helical flagellum (Higdon 1979), and the other two vectors, $\boldsymbol{D}^1(s, 0)$ and $\boldsymbol{D}^2(s, 0)$, are perpendicular to the tangent vector following the right-hand rule, i.e. normal and binormal vectors to the flagellum. Note that this initial configuration of the centreline and the triad of the helical flagellum are in the equilibrium state in the absence of

https://doi.org/10.1017/jfm.2018.799 Published online by Cambridge University Press

external forces, and that their deformation from the reference configuration gives rise to the internal energy and force.

Let $\boldsymbol{N}(s,\ t)$ and $\boldsymbol{F}(s,\ t)$ be the moment and the force, respectively, which are transmitted across a section of the rod at the Lagrangian coordinate s at time t. Let $\boldsymbol{f}(s,t)$ and $\boldsymbol{n}(s,t)$ be the applied force and the torque densities, respectively. Then the momentum and angular momentum balance equations are described as

$$0=\boldsymbol{f}+\frac{\partial \boldsymbol{F}}{\partial s}, \tag{2.3}$$

$$0=\boldsymbol{n}+\frac{\partial \boldsymbol{N}}{\partial s}+\left(\frac{\partial \boldsymbol{X}}{\partial s}\times \boldsymbol{F}\right), \tag{2.4}$$

where all the variables may be expanded in the basis of the orthonormal triad as follows:

$$\boldsymbol{F}=\sum_{i=1}^{3} F_i\boldsymbol{D}^i,\quad \boldsymbol{N}=\sum_{i=1}^{3} N_i\boldsymbol{D}^i,\quad \boldsymbol{f}=\sum_{i=1}^{3} f_i\boldsymbol{D}^i,\quad \boldsymbol{n}=\sum_{i=1}^{3} n_i\boldsymbol{D}^i. \tag{2.5a–d}$$

The constitutive relations are given by

$$N_i=a_i\left(\frac{\partial \boldsymbol{D}^j}{\partial s}\cdot\boldsymbol{D}^k-\Omega_i\right), \tag{2.6}$$

where (i,j,k) is any cyclic permutation of $(1,2,3)$, and

$$F_i=b_i\left(\boldsymbol{D}^i\cdot\frac{\partial \boldsymbol{X}}{\partial s}-\delta_{3i}\right),\quad i=1,2,3, \tag{2.7}$$

where δ_{3i} is the Kronecker delta. The coefficients a_1 and a_2 are the bending moduli, and a_3 is the twist modulus of the rod. The coefficients b_1 and b_2 are the shear moduli, and b_3 is the stretching modulus, which controls the degree of inextensibility of the rod. The strain twist vector $(\Omega_1,\ \Omega_2,\ \Omega_3)$ designates the intrinsic property of the elastic rod in which $\kappa\equiv\sqrt{\Omega_1^2+\Omega_2^2}$ is the intrinsic curvature and Ω_3 is the intrinsic twist of the rod of which the sign determines the helical handedness of the rod. Negative values of Ω_3 correspond to a left-handed helix and positive values of Ω_3 correspond to a right-handed helix. We assume that the helical rod is intrinsically left-handed throughout this work. The constitutive relations above can be derived from a variational argument of the elastic energy potential for the unconstrained version of the Kirchhoff rod (Lim *et al.* 2008):

$$E=\frac{1}{2}\int_0^L\left[\sum_{i=1}^{3} a_i\left(\frac{\partial \boldsymbol{D}^j}{\partial s}\cdot\boldsymbol{D}^k-\Omega_i\right)^2+\sum_{i=1}^{3} b_i\left(\boldsymbol{D}^i\cdot\frac{\partial \boldsymbol{X}}{\partial s}-\delta_{3i}\right)^2\right]\mathrm{d}s, \tag{2.8}$$

where $L=L_h+L_f$ is the total length of the rod, and (i,j,k) is any cyclic permutation of $(1,2,3)$. Note that, in the limit $b_3\to\infty$, the rod becomes completely inextensible. In this work, we choose a value of b_3 sufficiently large to make the rod almost inextensible and set $a_1=a_2$ which implies that the rod is isotropic.

2.2. *Cell body modelling: penalty method*

In order to model a cell body, we use the penalty idea introduced by Kim & Peskin (2007, 2016) to simulate the movement of a massive body interacting with a

https://doi.org/10.1017/jfm.2018.799 Published online by Cambridge University Press

surrounding fluid. We assume that the cell body is a rigid, hollow ellipsoid which is represented by two Lagrangian descriptions: one is denoted by $\boldsymbol{X}_b(q, r, t)$ and has no mass, and the other, which we denote by $\boldsymbol{Y}_b(q, r, t)$, carries all of the mass and is connected to $\boldsymbol{X}_b(q, r, t)$ by a system of stiff springs; see the right-bottom panel of figure 1. Here (q, r) are parameters for the ellipsoidal surface and t is time. The different points on the massive boundary $\boldsymbol{Y}_b(q, r, t)$ have no direct connection to the fluid and move together as a rigid body in a vacuum, with the only forces and torques applied on the body being the forces generated from the springs that connect the massless description to the massive description of the rigid body.

Since both the massless and massive descriptions are supposed to represent the same body, if a pair of corresponding boundary points moves apart, a restoring force appears in order to make them move close together. The restoring force $\boldsymbol{F}_b$ acting on the massless boundary is

$$\boldsymbol{F}_b(q, r, t) = K_b(\boldsymbol{Y}_b(q, r, t) - \boldsymbol{X}_b(q, r, t)), \tag{2.9}$$

where K_b is a constant. This defines the force density $\boldsymbol{F}_b$ which is applied by the massless component $\boldsymbol{X}_b(q, r, t)$ of the cell body to the fluid so that $\boldsymbol{F}_b(q, r, t)\,\mathrm{d}q\,\mathrm{d}r$ is the force transmitted to the fluid by the area element $\mathrm{d}q\,\mathrm{d}r$ of the cell body. By Newton's third law, a negative force density $-\boldsymbol{F}_b(q, r, t)$ acts on the rigid cell body.

In order to describe the rigid-body dynamics, let $\boldsymbol{Y}_{cm}(t)$ be the centre of mass of the body, and let $\{\boldsymbol{E}_1(t), \boldsymbol{E}_2(t), \boldsymbol{E}_3(t)\}$ be the orthonormal basis for a coordinate system fixed to the body with its origin at the centre of mass. Then the position corresponding to the material point (q, r) of the body can be written as

$$\boldsymbol{Y}_b(q, r, t) = \boldsymbol{Y}_{cm}(t) + c_1(q, r)\boldsymbol{E}_1(t) + c_2(q, r)\boldsymbol{E}_2(t) + c_3(q, r)\boldsymbol{E}_3(t). \tag{2.10}$$

After we introduce two notations – one is a 3×3 matrix $\mathcal{E}(t)$ of which the ith column is the 3×1 vector $\boldsymbol{E}_i(t)$, and the second is the 3×1 vector-valued function $\boldsymbol{C}(q, r)$ of which the ith component is $c_i(q, r)$ – we can rewrite the position of the cell body as

$$\boldsymbol{Y}_b(q, r, t) = \boldsymbol{Y}_{cm}(t) + \mathcal{E}(t)\boldsymbol{C}(q, r). \tag{2.11}$$

Since the coordinates are fixed to the body, the coefficients $c_i(q, r)$ and $\boldsymbol{C}(q, r)$ are independent of time.

Now the equations of motion of the rigid body $\boldsymbol{Y}_b(q, r, t)$ are composed of the translational motion of the centre of mass and the rotational motion of the whole body about the centre of mass. The translational motion can be described as follows:

$$\frac{\mathrm{d}\boldsymbol{Y}_{cm}}{\mathrm{d}t} = \boldsymbol{V}_{cm}(t), \tag{2.12}$$

$$M\frac{\mathrm{d}\boldsymbol{V}_{cm}}{\mathrm{d}t} = -\int \boldsymbol{F}_b(q, r, t)\,\mathrm{d}q\,\mathrm{d}r, \tag{2.13}$$

where $\boldsymbol{V}_{cm}(t)$ is the velocity of the centre of mass, and M is the total mass of the hollow cell body which can be computed by $M = \int m(q, r)\,\mathrm{d}q\,\mathrm{d}r$, where $m(q, r)$ is the mass density of the cell body. Here and in the following, any integral with respect to q, r is understood to extend over the whole of the immersed body, i.e. the surface of the ellipsoidal cell body.

The rotational motion of the cell body can be summarized as

$$\boldsymbol{T}(t) = \int (\boldsymbol{Y}_b(q, r, t) - \boldsymbol{Y}_{cm}(t)) \times (-\boldsymbol{F}_b(q, r, t))\,\mathrm{d}q\,\mathrm{d}r, \tag{2.14}$$

https://doi.org/10.1017/jfm.2018.799 Published online by Cambridge University Press

$$\frac{\mathrm{d}\boldsymbol{L}}{\mathrm{d}t} = \boldsymbol{T}(t), \tag{2.15}$$

$$\boldsymbol{\Omega}(t) = \mathcal{E}(t)\boldsymbol{I}_0^{-1}\mathcal{E}(t)^{\mathrm{T}}\boldsymbol{L}(t), \tag{2.16}$$

$$\frac{\mathrm{d}\boldsymbol{E}_i}{\mathrm{d}t} = \boldsymbol{\Omega}(t) \times \boldsymbol{E}_i(t), \quad i = 1, 2, 3, \tag{2.17}$$

where $\boldsymbol{T}$ and $\boldsymbol{L}$ represent the total torque acting on the cell body and its angular momentum, respectively, and $\Omega(t)$ is the angular velocity of the body. In (2.16), the time-independent matrix $\boldsymbol{I}_0$, which is called the initial moment of the inertial tensor, can be computed by $\boldsymbol{I}_0 = \int m(q, r)(\boldsymbol{C}^{\mathrm{T}}\boldsymbol{C}\boldsymbol{I}_3 - \boldsymbol{C}\boldsymbol{C}^{\mathrm{T}})\,\mathrm{d}q\,\mathrm{d}r$, where $\boldsymbol{I}_3$ is a 3×3 identity matrix. For the detailed derivation for the formula, the readers can refer to Kim & Peskin (2016).

Note that, if $\boldsymbol{X}_b(q, r, t)$ were given, equations (2.9)–(2.17) would be complete and give the rigid-body motion. In order to compute the unknown massless representation $\boldsymbol{X}_b(q, r, t)$ of the rigid body, we need to take into account the hydrodynamic interaction between $\boldsymbol{X}_b(q, r, t)$ and the fluid, which will be discussed later in § 2.4.

2.3. *Motor linking the hook and the cell body*

We equip the bottom end of the hook with a rotary motor which is also attached at the north pole of the ellipsoidal cell body: see the right-middle panel of figure 1. The motor turns either CW or CCW at a prescribed angular velocity ω and generates the twist which is transmitted along the flagellum to its free end and hence leads to the rotation of the whole helical filament.

Since the cell body and the hook are both moving in time and physically share the motor point at the north pole, it is not only necessary to connect the hook to the cell body through the motor point, but we also need to align the direction of the hook with the direction of the cell body at the motor point. To do this, let $\boldsymbol{X}(0, t)$ be the bottom end of the hook, $\{\boldsymbol{D}^1(0, t), \boldsymbol{D}^2(0, t), \boldsymbol{D}^3(0, t)\}$ be its associated orthonormal triad and $\boldsymbol{Y}_b^n(t)$ be the north pole of cell body at time t. We assume that the third basis $\boldsymbol{E}_3(t)$ of the body is in the same direction as $\boldsymbol{Y}_b^n(t) - \boldsymbol{Y}_{cm}(t)$. Notice that, if we initially choose the orthonormal basis to satisfy this condition, it continues to hold over time. Then we define the feedback force and moment densities as follows:

$$\boldsymbol{f}_m(t) = K_m^1(\boldsymbol{Y}_b^n(t) - \boldsymbol{X}(0, t)), \tag{2.18}$$

$$\boldsymbol{n}_m(t) = K_m^2(\boldsymbol{E}_3(t) \times \boldsymbol{D}^3(0, t)), \tag{2.19}$$

where K_m^1 and K_m^2 are sufficiently large constants.

The force density $\boldsymbol{f}_m(t)$ at the motor point is added to the force density $\boldsymbol{f}$ in (2.3) at the bottom end point of the hook $\boldsymbol{X}(0, t)$ and expresses that, if the two points $\boldsymbol{X}(0, t)$ and $\boldsymbol{Y}_b^n(t)$ move apart, a restoring force comes into play in order to make them move close together. The negative force density $-\boldsymbol{f}_m(t)$ should also be added to $\boldsymbol{F}_b(q, r, t)$ at $\boldsymbol{Y}_b^n(t)$ and affects the total force and torque on the cell body. The moment density $\boldsymbol{n}_m(t)$ at the motor point is added to the moment $\boldsymbol{n}$ in (2.4) at $\boldsymbol{X}(0, t)$, which expresses that, if the two vectors $\boldsymbol{D}^3(0, t)$ and $\boldsymbol{E}_3(t)$ are not aligned, a restoring moment appears in order to rotate the triad $\boldsymbol{D}^3(0, t)$ towards $\boldsymbol{E}_3(t)$ as close as possible. The negative moment $-\boldsymbol{n}_m(t)$ is also added to the total torque $\boldsymbol{T}(t)$ on the cell body.

Now we rotate the motor point at the frequency ω about the tangent vector $\boldsymbol{D}^3(0, t)$. This can be done by defining the orthonormal triad at the motor point $\boldsymbol{X}(0, t)$ as follows:

$$\boldsymbol{D}^i(0, t) = \mathcal{R}(\boldsymbol{D}^3(0, t))\boldsymbol{D}_{mot}^i(t), \quad i = 1, 2, \tag{2.20}$$

https://doi.org/10.1017/jfm.2018.799 Published online by Cambridge University Press

where $\mathcal{R}(\boldsymbol{D}^3(0,t))$ represents a rotational matrix to transform the unit vector $(0,0,1)$ to the unit vector $\boldsymbol{D}^3(0,t)=(T_1(t),T_2(t),T_3(t))$ and has the form

$$\begin{pmatrix} T_3(t)+T_2(t)^2/(1+T_3(t)) & -T_1(t)T_2(t)/(1+T_3(t)) & T_1(t) \\ -T_1(t)T_2(t)/(1+T_3(t)) & T_3(t)+T_1(t)^2/(1+T_3(t)) & T_2(t) \\ -T_1(t) & -T_2(t) & T_3(t) \end{pmatrix}. \tag{2.21}$$

The two orthonormal vectors $\boldsymbol{D}^i_{mot}(t)$, $i=1,2$, represent the vectors which are rotated at frequency ω from the two standard bases $(1,0,0)$ and $(0,1,0)$, respectively, and have the following forms:

$$\boldsymbol{D}^1_{mot}(t)=(\cos(2\pi\omega t),\sin(2\pi\omega t),0), \tag{2.22}$$

$$\boldsymbol{D}^2_{mot}(t)=(-\sin(2\pi\omega t),\cos(2\pi\omega t),0), \tag{2.23}$$

where t is the time in seconds and ω is the rotation rate in Hz. The sign of ω determines the direction of rotation, i.e. $\omega>0$ corresponds to CCW rotation and $\omega<0$ corresponds to CW rotation when the rod is viewed towards the motor from the helical filament. Note that we do not prescribe the dynamics (velocity and position) of the flagellum, which was done in the previous studies (Chwang & Wu 1971; Higdon 1979; Phan-Thien *et al.* 1987; Fujita & Kawai 2001). Instead, we rotate the triad only at the motor point, which is more realistic, and the rotation of the motor applies the torque to the hook and then to the helical filament which can rotate together.

2.4. *Regularized Stokes formulation*

The bacterium is immersed in a viscous fluid which is governed by the incompressible Stokes equations

$$0=-\nabla p+\mu\Delta\boldsymbol{u}+\boldsymbol{g}, \tag{2.24}$$

$$0=\nabla\cdot\boldsymbol{u}, \tag{2.25}$$

where μ is the fluid viscosity. The unknown variables $\boldsymbol{u}$, p and $\boldsymbol{g}$ are the fluid velocity, pressure and the external force per unit volume applied to the fluid, respectively, and they are functions of the fixed Cartesian coordinates $\boldsymbol{x}$ and the time t. The force density $\boldsymbol{g}$ in (2.24) is given as the regularized form

$$\begin{aligned}\boldsymbol{g}(\boldsymbol{x},t) \;=\; & \int_0^L(-\boldsymbol{f}(s,t))\psi_\epsilon(\boldsymbol{x}-\boldsymbol{X}(s,t))\,\mathrm{d}s+\frac{1}{2}\nabla\times\int_0^L(-\boldsymbol{n}(s,t))\psi_\epsilon(\boldsymbol{x}-\boldsymbol{X}(s,t))\,\mathrm{d}s \\ & +\int\boldsymbol{F}_b(q,r,t)\psi_\epsilon(\boldsymbol{x}-\boldsymbol{X}_b(q,r,t))\,\mathrm{d}q\,\mathrm{d}r,\end{aligned} \tag{2.26}$$

where the first two terms on the right-hand side are the force from the elastic rod (hook and filament), and the last term is the force contributed from the cell body. The radially symmetric blob function ψ_ϵ is defined as

$$\psi_\epsilon(\boldsymbol{r})=\frac{15\epsilon^4}{8\pi(|\boldsymbol{r}|^2+\epsilon^2)^{7/2}}, \tag{2.27}$$

where ϵ is the regularization parameter and $\boldsymbol{r}=\boldsymbol{x}-\boldsymbol{X}$ for a point $\boldsymbol{x}$ in the fluid (Cortez 2001; Olson *et al.* 2013). The blob function ψ_ϵ is a bell-shaped function

https://doi.org/10.1017/jfm.2018.799 Published online by Cambridge University Press

with infinite support and satisfies $\iiint_{\boldsymbol{R}^3} \psi_\epsilon(\boldsymbol{r})\,\mathrm{d}\boldsymbol{r} = 1$, spreading most of the force and moment within a ball with the radius ϵ with its centre at the rod $\boldsymbol{X}$ or at the body $\boldsymbol{X}_b$. Equation (2.26) describes how we apply the force and torque generated in the immersed body to the fluid, and this implies that the rate at which the immersed body works on the fluid is written in terms of the force and moment applied to the fluid (Lim *et al.* 2008).

Together with (2.3)–(2.7), (2.9)–(2.17) and (2.24)–(2.26), the coupled system of equations closes with the addition of the following equations:

$$\boldsymbol{w}(\boldsymbol{x}, t) = \tfrac{1}{2}\nabla \times \boldsymbol{u}(\boldsymbol{x}, t), \tag{2.28}$$

$$\frac{\partial \boldsymbol{X}(s, t)}{\partial t} = \boldsymbol{u}(\boldsymbol{X}(s, t), t), \tag{2.29}$$

$$\frac{\partial \boldsymbol{D}^i(s, t)}{\partial t} = \boldsymbol{w}(\boldsymbol{X}(s, t), t) \times \boldsymbol{D}^i(s, t), \quad i = 1, 2, 3, \tag{2.30}$$

$$\frac{\partial \boldsymbol{X}_b(q, r, t)}{\partial t} = \boldsymbol{u}(\boldsymbol{X}_b(q, r, t), t). \tag{2.31}$$

Equation (2.28) is the relation between the fluid angular velocity $\boldsymbol{w}$ and the fluid velocity $\boldsymbol{u}$, both of which are solved using a regularized Stokes formulation. The interaction between the elastic rod and the fluid is described in (2.29) and (2.30) which are the no-slip conditions for the velocity and the angular velocity, respectively. These equations imply that the centreline of the rod translates at the local fluid velocity and that the triad rotates at the local fluid angular velocity. See Olson *et al.* (2013) and Lee *et al.* (2014) for a more detailed description of both the mathematical formulation and its numerical scheme. The interaction between the cell body and the fluid is described in (2.31) which also represents the no-slip condition.

Table 1 shows the computational and physical parameters used in this paper. The fluid viscosity μ is the same as that of water. We compute the intrinsic strain vector $(\Omega_1, \Omega_2, \Omega_3)$ from the initial shape of the helical filament given in (2.1) and (2.2). Since the radius of the helical filament increases continuously from 0 to r_0, the intrinsic strain vector is also a variable function. The intrinsic curvature $\kappa = \sqrt{\Omega_1^2 + \Omega_2^2}$ and twist $\tau = \Omega_3$ given in table 1 correspond to the values of a helical filament with a constant radius r_0. Note that we use the exponent $k_E > 2$ in (2.2) and, thus, the majority of our filament model has an approximately constant helical radius r_0. The cell body is of the shape of a prolate spheroid which has a long axis denoted as body length, $2A$, and two short equal axes denoted as body width, $2B$. Note that the bending modulus of the relaxed hook is approximately 4 times smaller than that of the loaded hook. The relaxed state begins with the reversal of the motor from CW to CCW and lasts for a short period of time. The loss of the stiffness of the hook will be shown to be a crucial factor for the buckling of the hook. Table 1 presents parameter values of the prototype of our bacterium model. In the following sections, however, we vary those physical parameters pertaining to the filament, cell body and the fluid to investigate how these parameters affect the dynamics of swimming bacteria.

3. Results and discussion

3.1. *Numerical validation of the model*

In this section, we validate the present mathematical model of a single-flagellated bacterium by comparing our simulation results with those of Higdon (1979), who used slender-body theory for Stokes flow and an image system for the cell body.

https://doi.org/10.1017/jfm.2018.799 Published online by Cambridge University Press

Parameters (symbol)	Value
Fluid viscosity (μ)	10^{-6} g (μm s)$^{-1}$
Regularization parameter (ϵ)	$3\Delta s$
Time step (Δt)	2.5×10^{-9} s
Mesh width for flagellum (Δs)	0.03 μm
Helical radius of filament (r_0)	0.2371 μm
Helical pitch of filament (p_0)	1.49 μm
Curvilinear length of filament (l)	4.5 μm
Intrinsic curvature of filament (κ)	2.1085 μm^{-1}
Intrinsic twist of filament (τ)	2.1085 μm^{-1}
Bending modulus of filament ($a_1 = a_2 = a$)	0.04 g μm^3 s^{-2}
Twist modulus of filament (a_3)	0.04 g μm^3 s^{-2}
Shear modulus ($b_1 = b_2$)	2.0 g μm s^{-2}
Stretch modulus (b_3)	2.0 g μm s^{-2}
Length of hook (L_h)	0.105 μm
Bending modulus of relaxed hook (a_{relax})	0.0000725 g μm^3 s^{-2}
Bending modulus of loaded hook (a_{load})	0.0003 g μm^3 s^{-2}
Twist modulus of hook (a_3^{hook})	$1 \times a_3$ g μm^3 s^{-2}
Rotation rate of motor (ω)	450 Hz
Cell body length ($2A$)	2.4 μm
Cell body width ($2B$)	1.0 μm
Cell body density (m)	10^{-12} g μm^{-2}

TABLE 1. Computational and physical parameters.

As in Higdon (1979), we construct a bacterium with a spherical cell body of radius $A = 0.9$ μm and a left-handed helical flagellum of two different arc lengths $l = 4.5$ μm and 9 μm. A difference in the helical shape can be generated by changing the helical radius r_0, helical pitch p_0 and the linear length of the helix L_f while we fix $2\pi r_0/p_0 = 1$ and $p_0 k_E = 2\pi$. Figure 2(*a*) shows bacteria with four different configurations depending on the ratio of the flagellum length and the sphere radius, l/A, and the number of waves, $N_\lambda = L_f/p_0$. The motor in the model rotates CCW at the frequency ω when viewed from the flagellum towards the motor, which induces the forward swimming of the micro-organism because the flagellum is intrinsically left-handed and the wave propagates from the motor to the distal end of the flagellum (Lim & Peskin 2012; Ko *et al.* 2017). Since the vector $\boldsymbol{E}_3(t)$ is a unit vector from the centre of mass of the cell body to the north pole, we can compute the directional swimming speed of the cell body as

$$V_f(t) = -\boldsymbol{V}_{cm}(t) \cdot \boldsymbol{E}_3(t). \tag{3.1}$$

If $V_f > 0$, the bacterium swims forward, and if it is negative, the bacterium swims backward. Figure 2(*b*) shows the forward swimming speed $V_f(t)$ as a function of time for various values of l/A and N_λ. We can see that the bacteria reach steady forward swimming motions with small oscillations.

Now we define the average swimming speed $\overline{V}_f$ as the average value of the directional swimming speed $V_f(t)$ over time after the micro-organism reaches the steady swimming motion with small oscillations. Since there is an oscillatory motion of the cell body, $\boldsymbol{E}_3(t)$ is not perfectly aligned with the direction of the motion of

https://doi.org/10.1017/jfm.2018.799 Published online by Cambridge University Press

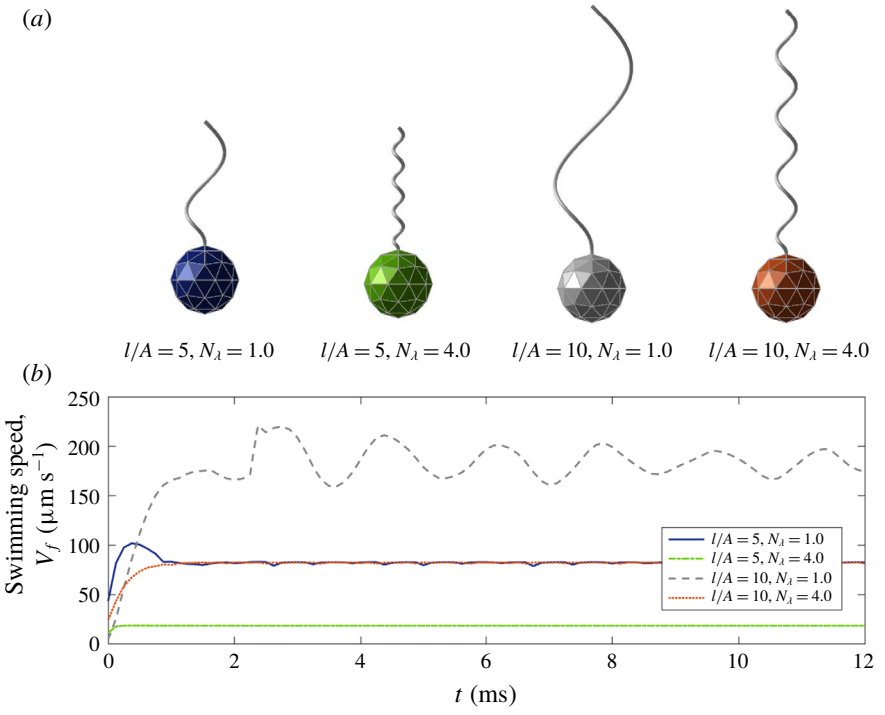


FIGURE 2. (Colour online) (*a*) The four different configurations of the model organism depending on l/A and $N_\lambda = L_f/p_0$, and (*b*) the corresponding swimming speeds $V_f(t)$ of the cell body as functions of time. The bacteria eventually reach steady forward swimming motions with small oscillations.

the cell. Thus, $V_f(t)$ is not equal to the swimming speed in the direction of average motion, and $\overline{V}_f$ is not equal to the net displacement of the cell body over the elapsed time. However, since the bacterium swims straight on average, $\overline{V}_f$ is very close to the forward (z-) directional displacement of the cell body over the elapsed time. Figure 3(*a*) shows the average swimming speed normalized by the linear wave speed $V = \omega p_0/(2\pi)$ of the rotating helical flagellum, i.e. $\overline{V}_f/V$ for two different ratios l/A and various values of N_λ. Our numerical results for the average swimming speed are in a good agreement with those in Higdon (1979) and Phan-Thien *et al.* (1987), which are almost identical.

The power consumption of the flagellum to move the whole body, which measures how efficient the swimming mechanism is, can be computed by the following formula:

$$\mathcal{P}(t) = \int_0^L \boldsymbol{f}(s,t) \cdot \boldsymbol{u}(\boldsymbol{X}(s,t),t)\,\mathrm{d}s. \tag{3.2}$$

Let $\overline{\mathcal{P}}$ be the power consumption averaged over time when the micro-organism reaches the steady swimming motion; then we can define the dimensionless power consumption η_0^{-1} by the following formula:

$$\eta_0^{-1} = \frac{\overline{\mathcal{P}}}{6\pi\mu A \overline{V}_f^2}. \tag{3.3}$$

https://doi.org/10.1017/jfm.2018.799 Published online by Cambridge University Press

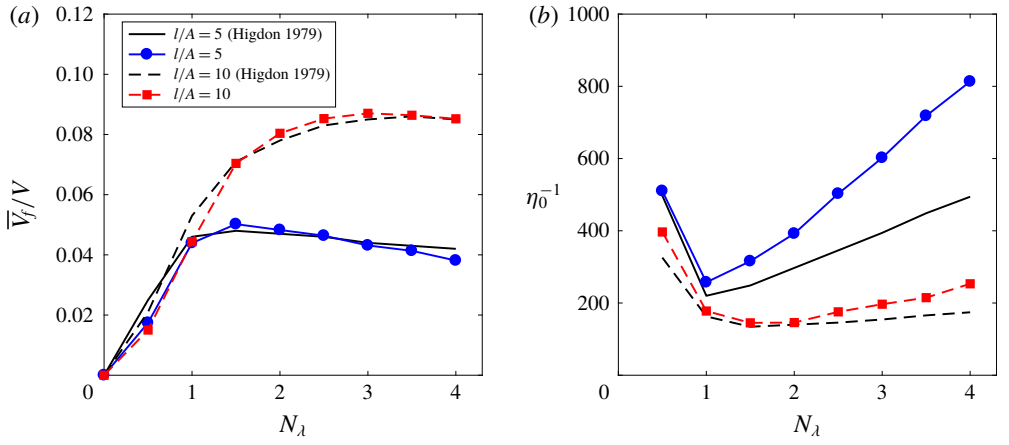


FIGURE 3. (Colour online) Normalized average forward swimming speed $\overline{V}_f/V$ (*a*) and non-dimensional power consumption η_0^{-1} (*b*) as functions of the number of waves N_λ. The curves compare our numerical results with those in Higdon (1979) for two different ratios of the flagellum length and the sphere radius $l/A = 5$ and 10.

Figure 3(*b*) shows the dimensionless power consumption η_0^{-1} in terms of N_λ for two different ratios of the flagellum length and the sphere radius $l/A = 5$ and 10. The power consumption of our mathematical model is generally larger than the data in Higdon (1979), which implies that more power is needed for the bacteria to swim forward in our model than the model in Higdon (1979). The reason for this discrepancy might lie in the difference in the properties of the rotating flagellum: whereas the flagellum model in Higdon (1979) is perfectly rigid and rotates as a rigid body, our flagellum model is flexible and rotates by the torque which is generated by the spinning motor and transmitted along the flexible flagellum.

Even though the power consumptions of our model are quantitatively different from the data in Higdon (1979), qualitative agreement is shown in figure 3(*b*). In particular, a higher value of ratio l/A requires a smaller power consumption for the forward swimming, and the power consumptions in both models achieve the optimal values approximately at $N_\lambda = 1$ for $l/A = 5$ and $N_\lambda = 1.5$ for $l/A = 10$.

3.2. *Forward and backward swimming motions*

V. alginolyticus swims straight backward and forward by rotating the motor CW and CCW, respectively. In order to see the bacterial motion along a straight line, a model bacterium adopts the physical and geometrical parameter values shown in table 1; see also figure 1 for the initial configuration of the model. Note that the single flagellum attached to the cell body is intrinsically left-handed. The motor first rotates CW till $t = 50$ ms and then switches to CCW rotation. Figure 4(*a*) shows the swimming motion of the bacterium at some selected times (see also supplementary movie 1 available at https://doi.org/10.1017/jfm.2018.799), and figure 4(*b*) shows the directional swimming speed $V_f(t)$ (solid line) and the head's rotational frequency ω_b (dashed line) as functions of time. The CW rotation of the motor induces the CW rotation of the left-handed flagellum which pushes the fluid in the forward direction and pulls the cell body in the backward direction, resulting in the straight backward bacterial swimming. The forward swimming driven by the CCW rotation of the motor can

https://doi.org/10.1017/jfm.2018.799 Published online by Cambridge University Press

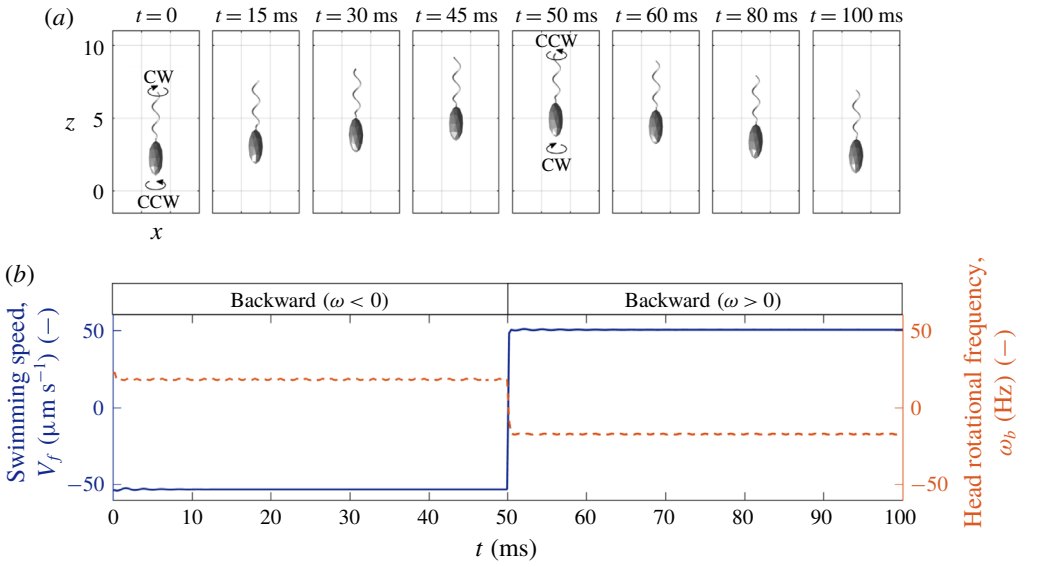


FIGURE 4. (Colour online) (*a*) The time evolution of backward and forward swimming motions: when the motor rotates CW (CCW), the cell body counter-rotates and the bacterium swims backward (forward). (*b*) The directional swimming speed (solid line) and the rotational frequency of the cell body (dashed line). The positive and negative signs of the cell body frequency correspond to CCW and CW rotations, respectively.

be explained in the similar manner. During the backward and forward runs, the cell body counter-rotates naturally to balance the torque.

Throughout this section, we use the bending modulus of the hook as a constant value at all times, i.e. $a_{hook} = a_{load} = 0.0003$ g μm^3 s^{-2}, which allows the bacterium to reverse the swimming direction quickly as the motor alternates its rotational direction. In reality, however, the bending modulus of the hook gets smaller right after the change of the rotational direction of the motor, i.e. $a_{load} > a_{hook} = a_{relax}$, which might induce a buckling instability of the hook. This case will be discussed separately in the next section.

It is known that *V. alginolyticus* swims faster in the backward direction than in the forward direction (Magariyama *et al.* 2001). Figure 4(*b*) confirms this experimental observation in which, although the motor rotates at the same magnitude of frequency, $\omega = \pm 450$ Hz, the swimming speed is -53.07 μm s^{-1} in the backward swimming and 50.22 μm s^{-1} in the forward swimming. It was also observed experimentally (Chwang & Wu 1971) that while the motor and hence the flagellum rotate in the same direction, the cell body rotates in the opposite direction with an approximate relation $\omega = -22\omega_b$ where ω_b is the rotational frequency of the cell body (Chattopadhyay & Wu 2009; Lauga & Powers 2009; Son *et al.* 2013). Figure 4(*b*) also shows that the cell body rotates at $\omega_b = 18.02$ Hz during the backward run with $\omega = -450$ Hz and it rotates at $\omega_b = -17.36$ Hz during the forward run with $\omega = 450$ Hz. In both cases, the ratio ω/ω_b is approximately -25.

We investigate the dependence of the swimming speed and the rotation rate of the cell body on various physical parameters. Each pair of panels in figure 5 shows the absolute value of the swimming speed, $|V_f|$ (*a*,*b*,*e*,*f*), and the ratio of the rotational frequencies of the motor and the cell body, ω/ω_b (*c*,*d*,*g*,*h*) in terms of four different

https://doi.org/10.1017/jfm.2018.799 Published online by Cambridge University Press

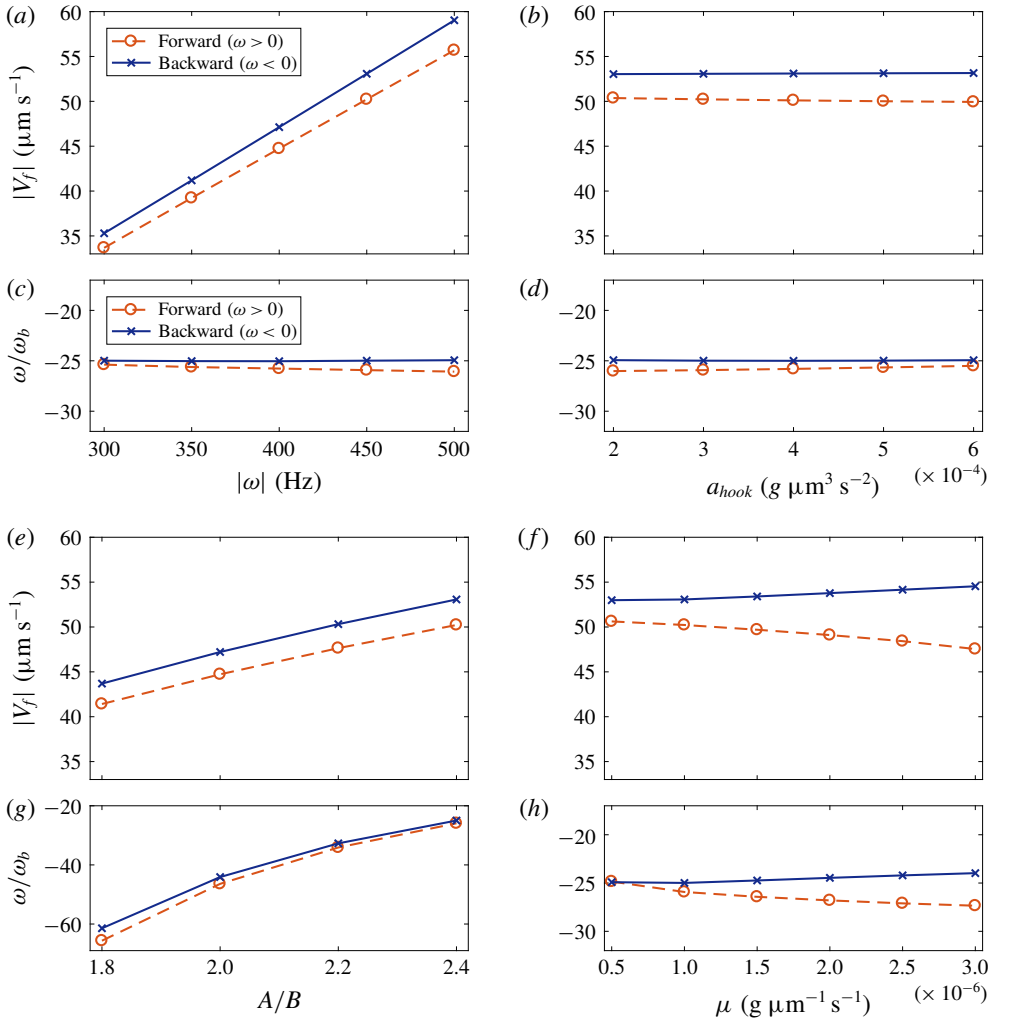


FIGURE 5. (Colour online) The swimming speed, $|V_f|$ (a,b,e,f), and the ratio of the rotational frequencies of the motor and the cell body, ω/ω_b (c,d,g,h) in terms of four different parameters: rotational frequency of the motor ω (a,c), bending modulus of the hook a_{hook} (b,d), cell body ratio A/B (e,g) and fluid viscosity μ (f,h). The lines with '○' and '×' indicate the forward and backward swimming modes, respectively.

parameters: rotational frequency of the motor ω (a,c), bending modulus of the hook a_{hook} (b,d), cell body ratio A/B (e,g) and fluid viscosity μ (f,h). When one of the parameters varies, all the other parameters are held fixed at the values given in table 1. The lines with '○' and '×' indicate the forward and backward swimming modes, respectively, and thus CCW and CW rotations of the flagellum, respectively.

Figure 5(a,c) shows that the swimming speed and the rotational frequency of the cell body increase linearly with the angular frequency of the motor and that the ratios of the rotational frequencies of the motor and the cell body stay approximately at a constant value, -25.0. The bending modulus of the hook a_{hook} has almost no influence on the swimming speed and the cell body rotation within the range of a_{hook} given in

https://doi.org/10.1017/jfm.2018.799 Published online by Cambridge University Press

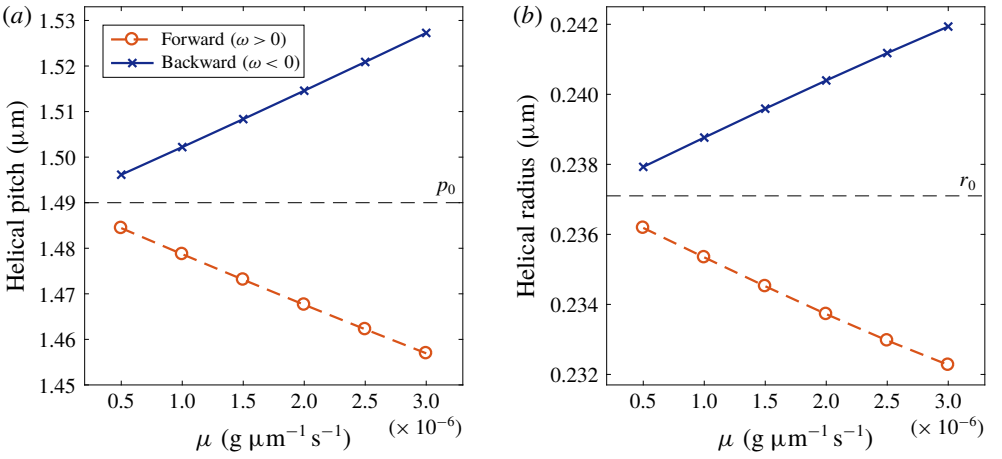


FIGURE 6. (Colour online) The measured values of the helical pitch (*a*) and the helical radius (*b*) of the flagellum in comparison with those of the initial flagellum in the equilibrium state (dashed lines). The bacterium swims forward and backward with $\omega = \pm 450$ Hz in a fluid with various viscosities.

figure 5(*b*,*d*). Note that, if a_{hook} is smaller than some critical value and the bacterium swims forward, the hook goes through a buckling instability; see the next section.

Figure 5(*e*,*g*) shows that the swimming speed and the rotational speed of the cell body increase as the cell body ratio A/B increases. In these simulations, we change the minor axis B only while the major axis A of the ellipsoidal body is fixed as a constant. As the ratio A/B increases and thus B decreases, the cell body becomes more slender and experiences a lower drag force from the fluid, which enables the cell body to translate and turn faster.

As the fluid viscosity μ increases, the linear and angular swimming speeds of the cell body increase slightly in the backward swimming mode, but they decrease to a relatively large extent in the forward swimming mode: see figure 5(*f*,*h*). This supports that the backward swimming speed is always larger than the forward swimming speed in the natural marine fluid even with the same magnitude of the motor frequency; see also the upper panel of each pair.

The difference in the swimming speeds depending on the swimming direction and the fluid viscosity is due to the change of the geometrical properties of the flexible flagellum. Figure 6 depicts the measured values of the helical pitch (*a*) and helical radius (*b*) of the flagellum when it swims forward ('○') and backward ('×') in a fluid with various viscosities in comparison with those of the initial flagellum in the equilibrium state (dashed lines). We can see that the helical pitch and radius become smaller in the forward swimming mode than those of equilibrated flagellum due to the compression while they become larger in the backward swimming mode due to the tension. These differences get larger as the fluid viscosity increases. Ko *et al.* (2017) demonstrated that the mean fluid flux generated by a rotating helical filament, which implies a swimming speed, depends proportionally on the helical pitch and radius. These proportional relations of the swimming speed with the helical radius and the helical pitch (only when the pitch is large enough) have also been observed in experiments (Rodenborn *et al.* 2013; Thawani & Tirumkudulu 2017). Thus, as the fluid viscosity increases, the swimming speed gets larger in the backward direction and

https://doi.org/10.1017/jfm.2018.799 Published online by Cambridge University Press

smaller in the forward direction. Since a faster swimming body experiences a larger drag force from the fluid, the angular swimming speed ω_b is inversely proportional to the linear swimming speed: see figure 5(*h*).

3.3. *Buckling instability and reorientation*

A monotrichous bacterium *V. alginolyticus* has a single left-handed helical filament with its bottom end being linked to a short flexible hook (Kawagishi *et al.* 1996; Kudo *et al.* 2005). It swims forward and backward by rotating the motor which is embedded in the cell body (Homma *et al.* 1996; Goto *et al.* 2005). Since there is no chiral transformation of the helical flagellum during locomotion, it can swim back and forth in a straight line unless the flagellum bends and flicks the cell body. Thus, buckling of the hook plays a significant role in reorientation of swimming direction and the chemotaxis of single-flagellated bacteria.

The hook alternates two states during swimming, loaded and relaxed states, and the two states are distinguished by two different bending rigidities of the hook such that the loaded hook is less flexible than the relaxed hook, i.e. $a_{load} > a_{relax}$. The bacterium swims backward by turning the motor CW while the hook is in the loaded state. Then it suddenly changes the rotational direction of the motor to CCW, which causes the bacterium to swim forward and the hook to be in the relaxed state. The compression of the hook due to the forward swimming and the more flexible hook in the relaxed state may trigger the buckling instability of the flagellum followed by the flick of the bacterium. After a short period of the flick for reorientation of the organism, the hook is again in the loaded state to be straight, and the organism runs steadily forward in a new direction (Son *et al.* 2013). This swimming pattern of the run–reverse–flick movement is typical in the marine motile bacteria.

In order to investigate the buckling instability of the flagellum, we choose the relaxed and loaded bending moduli of the hook as $a_{relax} = 0.0000725$ g μm^3 s^{-2} and $a_{load} = 0.0003$ g μm^3 s^{-2}, respectively, which are two or three orders of magnitude lower than that of the flagellar filament as reported in Son *et al.* (2013). Figure 7 shows the dynamical motion of the computational model for *V. alginolyticus* (see also supplementary movie 2) and the resulting variations that occur in the organism as it experiences buckling instability. The flagellar motor initially turns CW and the hook is under tension and thus the organism swims backward steadily. At $t = 20$ ms the motor reverses to CCW and the hook is under the relaxed state from $t = 20$ to $t = 50$ ms. During this time period, there occurs a buckling instability of the hook and the flicking of the cell body. At $t = 50$ ms, the hook becomes loaded again, and the helical filament begins to be aligned with the cell body. When the cell body and the filament are aligned completely, the bacterium swims forward steadily in a new direction. Figure 7(*a*) shows snapshots taken at six selected times during locomotion of the bacterium which are drawn in the actual size. Figure 7(*d*) illustrates its trajectory in three-dimensional space following the order of start–reverse–flick–end, in which the size of the bacterium is scaled down for a better visualization.

To investigate more quantitatively the buckling dynamics of the bacterium, we define the following two quantities: the alignment, $q(t)$, between the swimming direction and the cell body orientation which is defined as $q(t) = -(\boldsymbol{V}_{cm}(t) \cdot \boldsymbol{E}_3(t))/|\boldsymbol{V}_{cm}(t)|$, and the buckling angle, $\theta(t)$, which is defined by an angle between the cell body axis and the helical axis. We compute the helical axis as a vector from the motor point to the average value of the coordinates of the flagellum. Figure 7(*b,c*) shows the alignment $q(t)$ and the buckling angle $\theta(t)$ as functions of

https://doi.org/10.1017/jfm.2018.799 Published online by Cambridge University Press

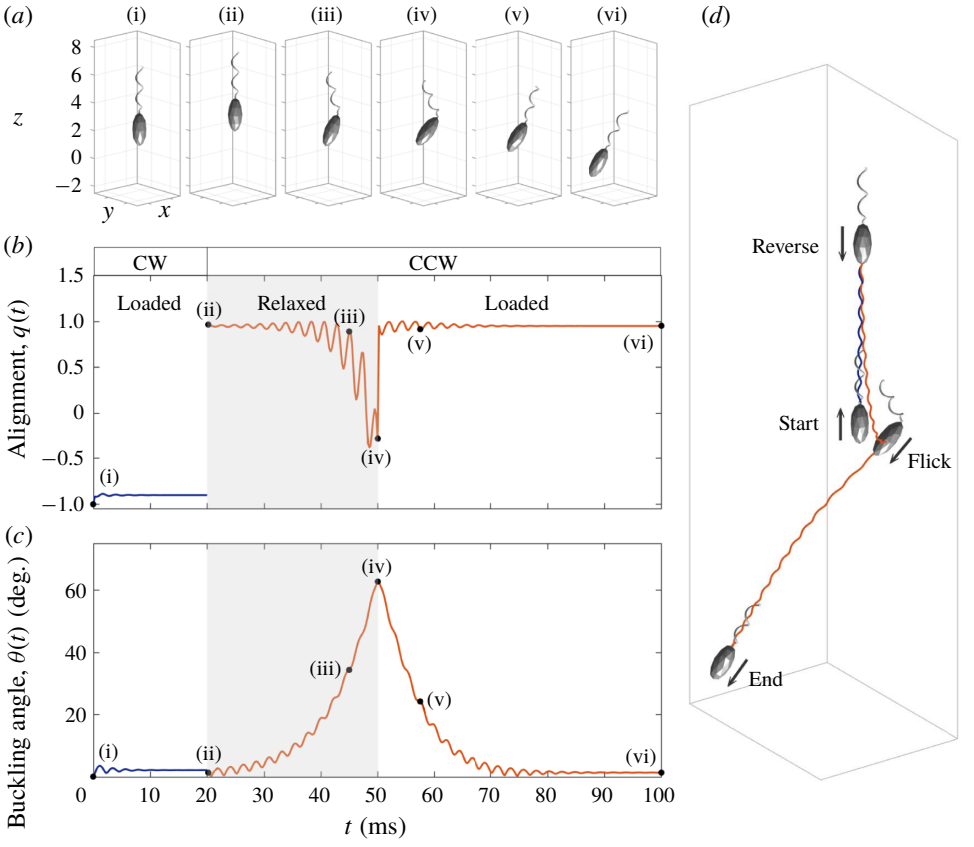


FIGURE 7. (Colour online) Snapshots at some chosen times (*a*), the trajectory (*d*) of the dynamical motion of *V. alginolyticus* and the time evolutions of the alignment $q(t)$ (*b*) and the buckling angle $\theta(t)$ (*c*). The trajectory of the organism follows the order of start–reverse–flick–end. The motor frequency changes from $\omega = -450$ Hz to 450 Hz at $t = 20$ ms. The bending modulus of the hook is given as $a_{relax} = 0.0000725$ g μm^3 s^{-2} in the relaxed state from $t = 20$ to $t = 50$ ms and $a_{load} = 0.0003$ g μm^3 s^{-2} in the loaded state.

time. The alignment $q(t)$ is around -1 (backward swimming) initially and changes into about $+1$ (forward swimming) at $t = 20$ ms. Then the flick begins approximately at $t = 25$ ms and lasts up to $t = 50$ ms, which is characterized by the deviation of $q(t)$ from ± 1. Then the alignment $q(t)$ reaches again $+1$ after $t = 50$ ms, which indicates that the swimming direction and the cell body orientation are aligned again. The buckling angle $\theta(t)$ is around 0 initially, which implies that the cell body axis and the helical axis are well aligned, and increases up to 63° during the relaxed state of the hook from 20 to 50 ms. Then it begins to decrease after the return of the hook to the loaded state at $t = 50$ ms and eventually gets close to 0 at approximately $t = 80$ ms. This swimming pattern of our mathematical model of *V. alginolyticus* is in a good agreement with the experimental observation reported in Son *et al.* (2013).

During backward swimming, the thrust from the flagellum and the drag on the cell body occur in opposite directions and repel away from one another, and thus the hook is under tension. In contrast, during forward swimming, the thrust and drag

https://doi.org/10.1017/jfm.2018.799 Published online by Cambridge University Press

attract one another and thus the hook is under compression. The compression of the hook triggers the buckling of the hook followed by the flicks of the bacterium, which results in reorientation of the cells. It is known that the hook of *V. alginolyticus* is a straight, hollow, slender rod with a length of approximately 100 nm and the bending modulus of the hook is 2–3 orders of magnitude smaller than that of the helical filament (Takano *et al.* 2003; Son *et al.* 2013). Thus, the hook can be easily bent when it is compressed. Euler beam theory (Timoshenko 1961; Son *et al.* 2013) predicts that a slender rod under axial and torsional loadings buckles when

$$F_h/F_{cr} + (T_h/T_{cr})^2 > 1, \tag{3.4}$$

where F_h and T_h are the typical axial force and torque acting on the rod, respectively, $F_{cr} = \pi^2 a_{hook}/L_h^2$ is the critical load and $T_{cr} = 2\pi a_{hook}/L_h$ is the critical torque for buckling of the rod.

In our mathematical model, the axial load F_h and the torque T_h acting on the hook can be computed by the following formula:

$$F_h(t) = -\boldsymbol{f}(0, t) \cdot \boldsymbol{D}^3(0, t)\Delta s; \quad T_h(t) = -\boldsymbol{n}(0, t) \cdot \boldsymbol{D}^3(0, t)\Delta s, \tag{3.5a,b}$$

where $\boldsymbol{f}(0, t)$, $\boldsymbol{n}(0, t)$ and $\boldsymbol{D}^3(0, t)$ are force density, moment density and the unit tangential vector, respectively, at the end point of the hook. Note that the negative sign makes the compression (tension) positive (negative).

Figure 8(*a–d*) illustrates the load F_h (upper) and the torque T_h (middle) as functions of time when the bacterium swims in the forward direction at two different rotation rates of the motor, $\omega = 300$ Hz (*a,c*) and 450 Hz (*b,d*). For each rotation rate, we display time evolutions of the load and torque for three different values of the bending modulus of the hook: $a_{hook} = 0.0001$ g μm^3 s^{-2} (solid lines), 0.000175 g μm^3 s^{-2} (dashed lines) and 0.00025 g μm^3 s^{-2} (dotted lines). Here, all the other parameters are held fixed at the values given in table 1. We can see that, when the bending modulus of the hook a_{hook} is larger than some critical values which depend on the rotational frequency of the motor, the load F_h and the torque T_h on the hook approach almost the same constant values independent of a_{hook}. However, when the motor turns faster or the bending modulus of the hook is smaller than the critical value, there occurs a buckling instability which is indicated by the deviation of the solid line from the other lines as shown in figure 8(*b,d*).

Collectively, figure 8(*e*) shows the separation of the stable ('○') and unstable ('×') regions of the hook as the bending modulus of the hook and motor frequency are varied. It appears that there exists a critical value of the bending modulus of the hook which increases linearly with the motor frequency. While the bending modulus of the hook is fixed, as the rotational frequency of the motor ω increases up to the critical threshold, the load F_h and torque T_h increase together in the forward swimming mode. These increments finally drive the hook into the region of the buckling instability.

While the motor frequency is fixed, each bending modulus above the critical value allows no buckling and induces limiting constant values of the force and torque acting on the hook. Figure 8(*f*) displays the mean of the limiting constant values of the load F_h ('○') and the torque T_h ('×'), when there is no buckling instability. In a low Reynolds number flow, the load F_h and torque T_h on the hook are linearly proportional to the swimming speed of the cell body (see the supplementary article of Son *et al.* 2013). Since the swimming speed increases linearly with the rotational frequency of the motor as shown in figure 5(*a*), the limiting constant values of the

https://doi.org/10.1017/jfm.2018.799 Published online by Cambridge University Press

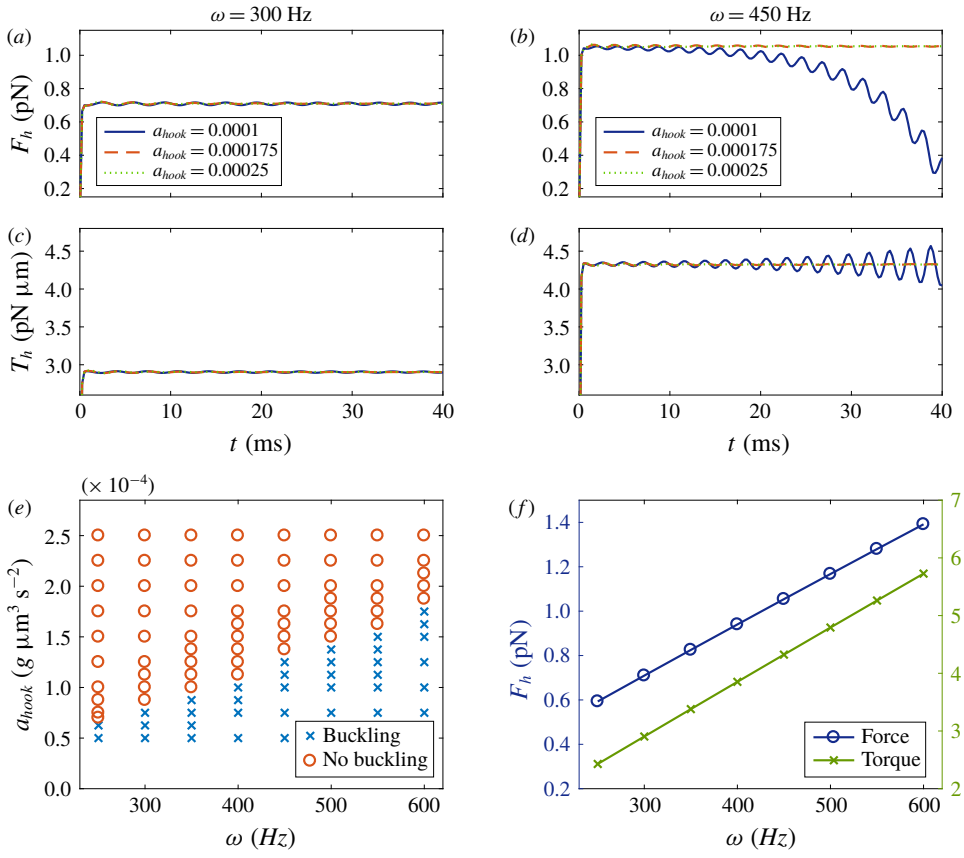


FIGURE 8. (Colour online) The axial load F_h (*a*,*b*) and torque T_h (*c*,*d*) as functions of time when the bacterium swims in the forward direction at two different rotation rates of the motor, $\omega = 300$ Hz (*a*,*c*,*e*) and 450 Hz (*b*,*d*,*f*). The bending modulus of the hook is given as $a_{hook} = 0.0001$ g μm^3 s^{-2} (solid lines), 0.000175 g μm^3 s^{-2} (dashed lines) and 0.00025 g μm^3 s^{-2} (dotted lines). The load F_h and torque T_h approach almost constant values except for the case with $a_{hook} = 0.0001$ g μm^3 s^{-2} and $\omega = 450$ Hz, in which case the hook buckles. Panel (*e*) classifies the region into the stable ('○') and unstable ('×') hooks as the bending modulus of the hook and the motor frequency are varied. The mean values of the limiting constant values of the load F_h ('○') and the torque T_h ('×') are displayed in terms of the rotational frequency of the motor (*f*).

load F_h and torque T_h are linearly proportional to the rotational frequency of the motor, as confirmed by our simulations.

The occurrence of buckling of the hook can be predicted by Euler beam theory (3.4). For example, since our model sets $a_{hook} = 0.0000725$ g μm^3 s^{-2} and $L_h = 0.105$ μm, the critical thresholds are given as $F_{cr} = 64.9$ pN and $T_{cr} = 4.34$ pN μm. With these particular values, figure 9(*a*) draws the buckling instability diagram of the hook with the solid parabola corresponding to $F_h/F_{cr} + (T_h/T_{cr})^2 = 1$. The markers indicate data points of axial forces and torques corresponding to nine different rotation rates of the motor from our simulations. According to the diagram, the critical frequency of the motor that separates stable from unstable hooks is expected to be approximately $\omega = 450$ Hz. However, this theoretical prediction for the buckling instability does not

https://doi.org/10.1017/jfm.2018.799 Published online by Cambridge University Press

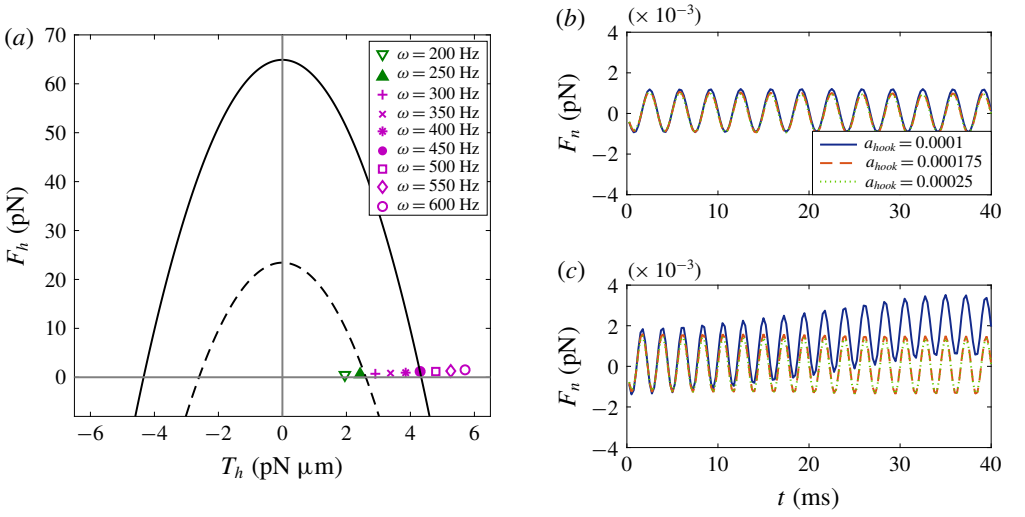


FIGURE 9. (Colour online) (*a*) Stable (no buckling) and unstable (buckling) regions separated by $F_h/F_{cr} + (T_h/T_{cr})^2 = 1$ (solid arc) and $F_h/F_{cr} + (T_h/T_{cr})^2 = 0.36$ (dashed arc) with the markers representing forces and torques in the cases of nine different motor frequencies. The critical loads for the solid curve are determined by $a_{hook} = 0.0000725$ g μm^3 s^{-2} and $L_h = 0.105$ μm. (*b*,*c*) One of the normal components of force, F_n, as a function of time for two different frequencies, $\omega = 300$ Hz (*b*) and 450 Hz (*c*), and three different bending moduli of the hook: $a_{hook} = 0.0001$ g μm^3 s^{-2} (solid lines), 0.000175 g μm^3 s^{-2} (dashed lines) and 0.00025 g μm^3 s^{-2} (dotted lines).

match with our numerical results shown in figure 8(*e*), in which the hook is buckled even when $\omega = 300$ Hz.

A possible reason for this discrepancy is that the beam theory uses the typical axial force and torque acting on the rod only in the direction along the rod (tangential direction), without taking into account the normal direction. When the organism moves forward by the rotation of the hook and flagellum, however, the force and torque in the direction perpendicular to the hook might be so large that they affect the condition for the buckling instability. Figure 9(*b*,*c*) illustrates one of the normal components of the load, denoted by F_n, as a function of time when the motor frequency is given as $\omega = 300$ Hz (*b*) and 450 Hz (*c*), and the bending modulus of the hook is given as $a_{hook} = 0.0001$ g μm^3 s^{-2} (solid lines), 0.000175 g μm^3 s^{-2} (dashed lines) and 0.00025 g μm^3 s^{-2} (dotted lines). Only when $\omega = 450$ Hz and $a_{hook} = 0.0001$ g μm^3 s^{-2}, does buckling of the hook occur: see the deviation of the solid line in (*c*) panel. Even though the normal forces are sinusoidal and have a mean of almost 0, their amplitudes are as large as the corresponding tangential loads shown in figure 8(*a*,*b*) and hence might impact on the buckling instability. Using the data shown in figure 8(*e*,*f*), we can derive a new prediction that the hook buckles when

$$F_h/F_{cr} + (T_h/T_{cr})^2 \gtrapprox 0.36, \tag{3.6}$$

which is represented as the dashed parabola in figure 9(*a*).

The buckling angle, which might determine the new swimming direction of the bacterium after flicks, can be dependent on the physical properties of the hook, flagellum and cell body. In order to first investigate the dependence of the buckling

https://doi.org/10.1017/jfm.2018.799 Published online by Cambridge University Press

angle and the swimming direction on the properties of the hook, we vary the following physical parameters of the hook: the relaxed bending modulus a_{relax}, the loaded bending modulus a_{load} and the twist modulus a_3^{hook}. The other parameter values are kept the same as in table 1. The motor turns CW at $\omega = -450$ Hz until $t = 20$ ms and rotates CCW at $\omega = 450$ Hz when $t > 20$ ms. The hook is in the loaded state at all times except for the time interval (20 ms, 50 ms), when it is in the relaxed state.

We measure the swimming direction of the organism using the deviation angle $\theta_z(t)$ of the cell body axis from the positive z-direction which is computed as $\theta_z(t) = \cos^{-1}(\boldsymbol{E}_3(t) \cdot (\boldsymbol{e}_3))$, where $\boldsymbol{e}_3$ is the standard unit vector in the positive z-direction. Since the vector from the centre to the north pole of the cell body is initially aligned with $\boldsymbol{e}_3$, the forward and backward runs both give rise to $\theta_z = 0°$, if there is no change of swimming direction. After buckling of the hook and flicking of the cell body are complete, since the cell body axis and the helical axis are well aligned in the loaded state, the organism reorients and swims forward steadily with a new value of θ_z.

Figure 10(*a*) shows the time evolution of buckling angles for various bending moduli of the relaxed hook ranging from $a_{relax} = 0.00007$ to 0.00012 g μm^3 s^{-2}, while $a_{load} = 0.0003$ g μm^3 s^{-2} and $a_3^{hook} = a_3$ are fixed. We can see that the maximum buckling angle depends inversely on the bending modulus of the relaxed hook, which is comparable to the results in Park *et al.* (2017). When a_{relax} is larger than 0.0001 g μm^3 s^{-2}, the buckling angle is so small that the hook is considered to be stable and no buckling occurs. The deviation angle θ_z is closely related to the buckling angle as shown in figure 10(*b*) in which we draw the constant value of the deviation angle obtained when the organism swims steadily in one direction after the buckling of the hook and the flicking of the cell body are complete. It is shown that the steady deviation angle θ_z is also inversely proportional to the bending modulus of the relaxed hook. In particular, when $a_{relax} = 0.00007$ g μm^3 s^{-2}, the maximum buckling angle is almost 90° and the steady deviation angle is approximately 42°.

Figure 10(*c*,*d*) depicts the time evolution of buckling angles (*c*) and the steady deviation angles (*d*) for various bending moduli of the loaded hook ranging from $a_{load} = 0.0002$ to 0.0004 g μm^3 s^{-2}, while $a_{relax} = 0.0000725$ g μm^3 s^{-2} and $a_3^{hook} = a_3$ are fixed. Since the buckling threshold depends only on the relaxed bending modulus a_{relax}, the buckling instability occurs independently of the loaded bending modulus a_{load} (Son *et al.* 2013; Park *et al.* 2017). However, the loaded bending modulus can change the maximum buckling angle and vary the time elapsed for the restoration of the buckling angle. In spite of these differences in the detailed behaviour of the buckling angle, the steady deviation angles θ_z, and thus the swimming directions differ only slightly as the bending modulus of the loaded hook is varied: see figure 10(*d*).

We also investigate the effect of the twist modulus of the hook a_3^{hook} while the bending moduli of the hook in the two different states are fixed as $a_{relax} = 0.0000725$ g μm^3 s^{-2} and $a_{load} = 0.0003$ g μm^3 s^{-2}. It is shown in figure 10(*e*) that the buckling angle is almost independent of the twist modulus of the hook. This result follows well the criterion for the buckling instability in (3.4) which does not depend on the twist modulus of the hook. Since the pattern of the buckling angles is similar, the new swimming directions are also similar, as shown in figure 10(*f*).

g

Figure 11(*a*,*b*) shows buckling angles as functions of time (*a*) and the steady deviation angles (*b*) for various rotational frequencies of the motor. As the motor frequency increases above 350 Hz, the buckling angle and the steady deviation angle increase substantially. However, when the motor rotates at a rate below 350 Hz, the buckling and deviation angles are so small that the new swimming direction is almost

https://doi.org/10.1017/jfm.2018.799 Published online by Cambridge University Press

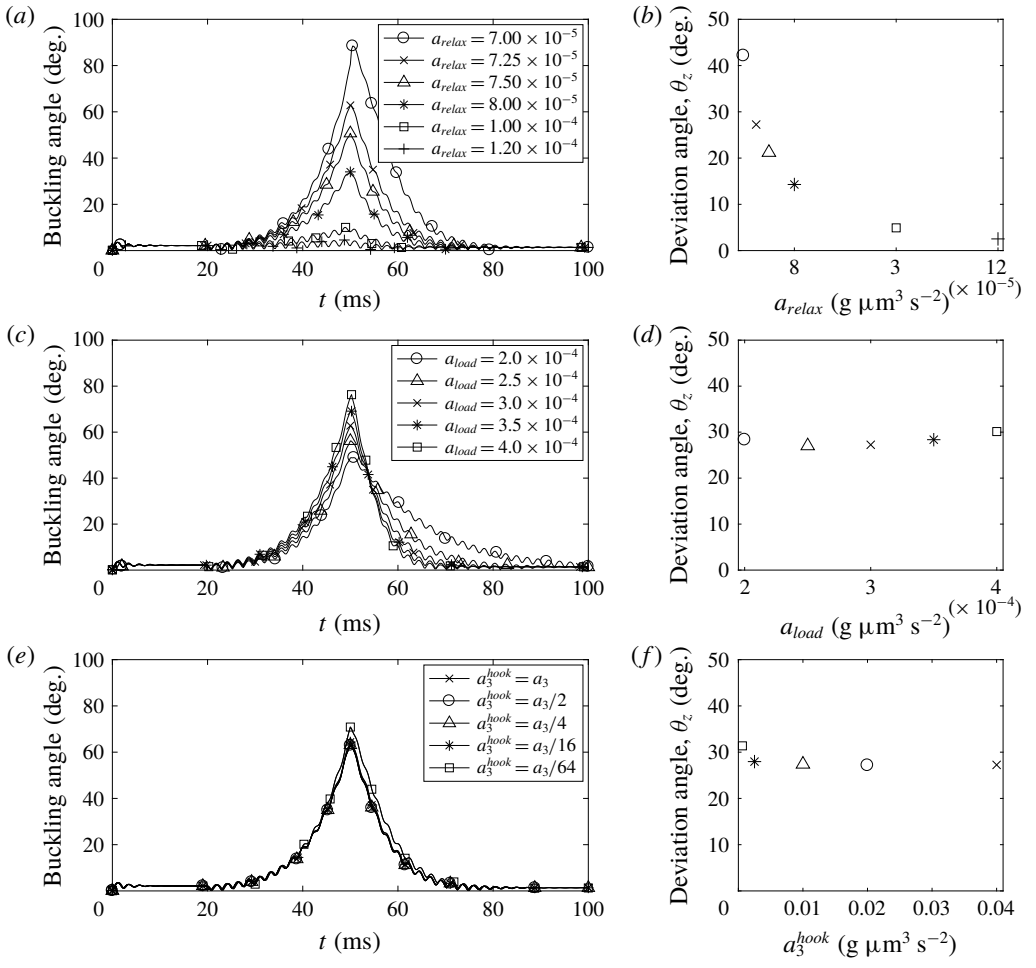


FIGURE 10. Buckling angle (*a*,*c*,*e*) and steady deviation angle (*b*,*d*,*f*) with various relaxed and loaded bending moduli and twist moduli of the hook. Relaxed bending modulus of the hook varies from 0.00007 to 0.00012 g μm^3 s^{-2} in (*a*,*b*), the loaded bending modulus of the hook is changed from 0.0002 to 0.0004 g μm^3 s^{-2} in (*c*,*d*), and the twist modulus of the hook is changed to be 1–64 times smaller than that of the helical filament in (*e*,*f*). The motor turns CW at $\omega = -450$ Hz until $t = 20$ ms and rotates CCW at $\omega = 450$ Hz when $t > 20$ ms. The hook is in the loaded state at all times except for 20 ms $< t <$ 50 ms, when it is in the relaxed state.

aligned with the old swimming direction, although the hook buckles very slightly and is unstable, as observed in figure 11(*a*). Such small deviations might not be noticeable in experimental settings.

The buckling angle and the steady swimming direction also depend on the mass density of the cell body: see figure 11(*c*,*d*). As the mass density m increases, since the total mass M and the moment of inertial tensor $\boldsymbol{I}_0$ increase, which makes it more difficult for the cell body to move and flick, both the maximum buckling angle and the steady deviation angle decrease. When the mass density is smaller than $m = 10^{-10}$ g μm^{-2}, the buckling angle and the steady deviation angle remain almost

https://doi.org/10.1017/jfm.2018.799 Published online by Cambridge University Press

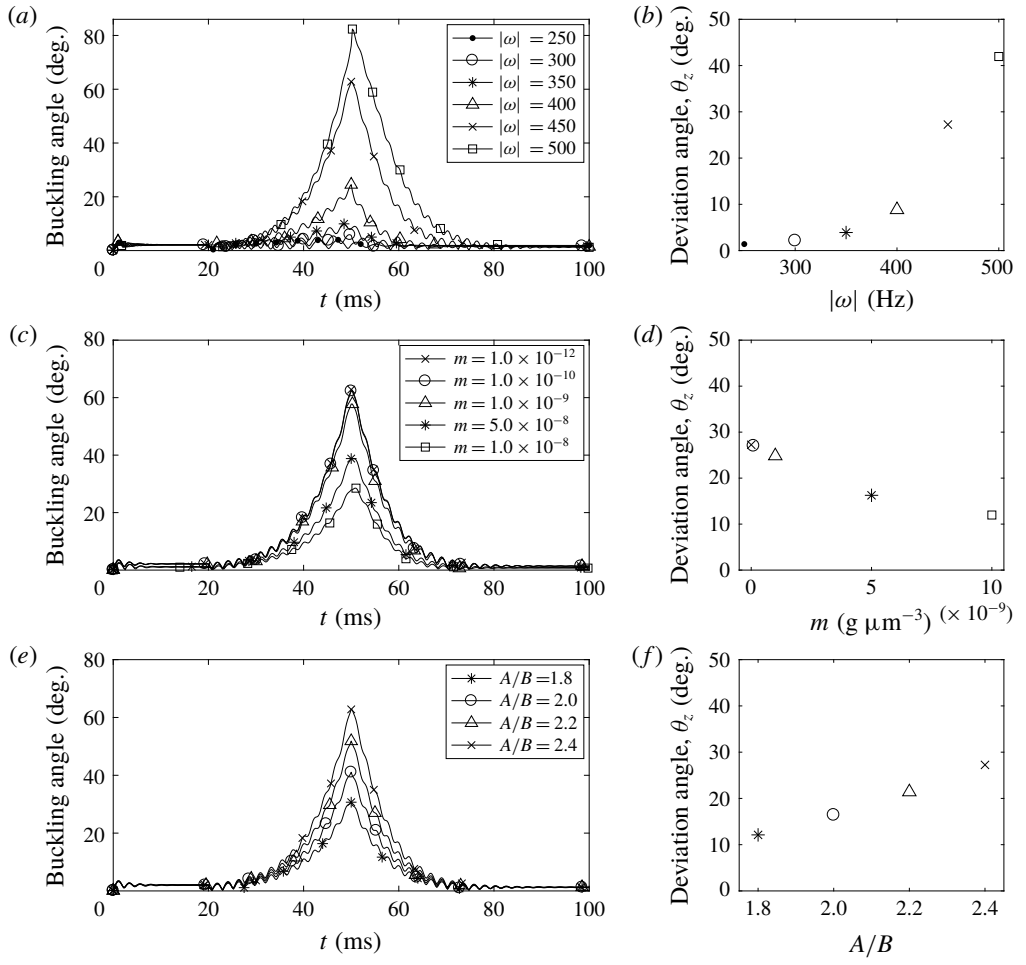


FIGURE 11. Buckling angle (*a,c,e*) and deviation angle (*b,d,f*) with various rotational frequencies of the motor ω (*a,b*), mass densities of the cell body m (*c,d*) and the body ratios A/B (*e,f*). The other parameters are the same as those in table 1.

the same. Since the total mass of a cell body can be considered as the sum of the mass of the fluid inside the cell body and the mass of its surface, its mass density is approximately 6–50 000 times larger than the surrounding fluid density based on the data in figure 11(*c,d*). One might think that these values are unrealistically large compared to the density of a real bacterium which is known to be slightly larger than that of water (Weng *et al.* 2011; Lewis, Craig & Senecal 2014). However, we find that the motion of the bacterium is independent of the mass density m of the cell body when it is smaller than 10^{-11} g μm^{-2}. Especially, the run–reverse–flick movement of the bacterium is almost the same whenever m is smaller than 10^{-11} g μm^{-2}.

Figure 11(*e,f*) shows that the maximum buckling angle (*e*) and the steady deviation angle (*f*) increase when the cell body ratio A/B increases. Note that we change the ratio A/B while the major axis A of the ellipsoidal body is fixed as a constant. Thus, as the ratio A/B increases, the short axis B decreases, since the drag force on the

https://doi.org/10.1017/jfm.2018.799 Published online by Cambridge University Press

cell body decreases, which makes it easier for the cell body to move and flick, the maximum buckling angle and the steady deviation angle increase.

4. Discussion and conclusions

We present a comprehensive model for a single-flagellated bacterium which includes an ellipsoidal cell body and a flagellum composed of an embedded motor, a compliant hook and an elastic helical filament. This mathematical model features: (i) the interaction between the cell body and the flagellum; (ii) the compliant hook that links the rotary motor to the filament working as a universal joint to transmit the motor rotation; (iii) the elastic helical flagellum inducing the translation–rotation coupling; and finally (iv) the interaction between the cell and its surrounding viscous fluid. Our model applies the motor-driven force alone to generate the helical wave propagation along the flagellum which results in the cell movement. We use Kirchhoff rod theory to model the elastic helical flagellum together with the hook and employ the penalty method to describe the dynamics of the rigid cell body. The hydrodynamic interaction between the fluid and the cell is represented by the regularized Stokes formulation.

Our simulation results on the average swimming speed and power efficiency of the cell, depending on the ratios of l/A and N_λ, are comparable with those of the previous studies based on the resistive-force theory and the slender-body theory (Higdon 1979; Phan-Thien *et al.* 1987) although there is a quantitative difference in power efficiency. In fact, this difference arises because the driving force in our model is applied only at the motor, as observed in nature, instead of rotating the whole flagellum as a rigid body, as done in the previous works. We further confirm that the aspect ratio of the cell body plays a significant role in determining the swimming speed and the counter-rotation rate of the cell body.

It is known that the helical filament of *V. alginolyticus* is intrinsically and permanently left-handed. This implies that, when the motor turns CCW, the helical wave propagates from the motor to the distal end of the filament and thus pumps the fluid away from the cell body, which results in the forward run. In contrast, when the motor turns CW, the helical wave propagates toward the motor and thus pulls the cell backward, which results in the backward run. In the absence of the buckling of the hook, the forward and backward runs of the cell in this work are consistent with the previous studies of rotating flagella even in the absence of the cell body (Kim *et al.* 2003; Lim & Peskin 2012; Park *et al.* 2017).

A monotrichous bacterium with a single left-handed helical flagellum can buckle and reorient by switching the rotational direction of the motor from CW to CCW, and the degrees of buckling and reorientation depend on the rotational frequency of the motor, elastic properties of the hook and physical and geometrical properties of the cell body. In particular, Euler's beam theory evaluates a buckling condition with the fixed bending modulus of the hook and the hook length, and predicts a critical motor frequency that separates stable hooks from unstable ones. The critical threshold in theory, however, turns out to be different from the simulated critical motor frequency. One reason for this discrepancy is that, whereas the beam theory considers the axial and torsional loadings only, the hook in our model is clamped or hinged on the wall of the cell body that can freely move, and thus the load perpendicular to the axial direction might facilitate the hook's buckling.

Variations in the physical and geometrical properties of the hook and the cell body demonstrate how these parameters affect the buckling angle and the new swimming direction after the buckling of the hook and the flick of the bacterium by

https://doi.org/10.1017/jfm.2018.799 Published online by Cambridge University Press

measuring the buckling angle and deviation angle. Our simulation results show that the relaxed bending modulus affects the buckling angle much more than the twist and loaded bending moduli of the hook. This result is consistent with a previous study on rotating flagella (Park *et al.* 2017), in which the maximum buckling angle is inversely proportional to the bending modulus of the relaxed hook. The change of properties of the cell body also makes a significant difference in the buckling dynamics. For a heavier cell body, the cell turns with a lesser degree. For a more slender cell body, the cell turns with a larger degree, which may allow bacteria with a rod-shaped cell body to have more directional freedom than ones with a spherical cell body.

Acknowledgements

Y.K. was supported by National Research Foundation of Korea Grant funded by the Korean Government (grant no. 2017R1E1A1A03070636), and S.L. was supported by National Science Foundation grant no. DMS-1410886 and the Charles Phelps Taft Research Center at University of Cincinnati, USA.

Supplementary movies

Supplementary movies are available at https://doi.org/10.1017/jfm.2018.799.

REFERENCES

BERG, H. C. 2003 The rotary motor of bacterial flagella. *Annu. Rev. Biochem.* **72** (1), 19–54.

BERG, H. C. & ANDERSON, R. A. 1973 Bacteria swim by rotating their flagellar filaments. *Nature* **245**, 380–382.

BLOCK, S. M., BLAIR, D. F. & BERG, H. C. 1989 Compliance of bacterial flagella measured with optical tweezers. *Nature* **338**, 514–518.

BLOCK, S. M., BLAIR, D. F. & BERG, H. C. 1991 Compliance of bacterial polyhooks measured with optical tweezers. *Cytometry* **12** (6), 492–496.

CHATTOPADHYAY, S. & WU, X. L. 2009 The effect of long-range hydrodynamic interaction on the swimming of a single bacterium. *Biophys. J.* **96** (5), 2023–2028.

CHWANG, A. T. & WU, T. Y. 1971 A note on the helical movement of micro-organisms. *Proc. R. Soc. Lond.* B **178** (1052), 327–346.

CORTEZ, R. 2001 The method of regularized Stokeslets. *SIAM J. Sci. Comput.* **23** (4), 1204–1225.

FLYNN, T. S. & MA, J. 2004 Theoretical analysis of twist/bend ratio and mechanical moduli of bacterial flagellar hook and filament. *Biophys. J.* **86** (5), 3204–3210.

FUJITA, T. & KAWAI, T. 2001 Optimum shape of a flagellated microorganism. *JSME Intl J.* **44** (4), 952–957.

FURUNO, M., ATSUMI, T., YAMADA, T., KOJIMA, S., NISHIOKA, N., KAWAGISHI, I. & HOMMA, M. 1997 Characterization of polar-flagellar-length mutants in *Vibrio alginolyticus*. *Microbiology* **143** (5), 1615–1621.

GOTO, T., NAKATA, K., BABA, K., NISHIMURA, M. & MAGARIYAMA, Y. 2005 A fluid-dynamic interpretation of the asymmetric motion of singly flagellated bacteria swimming close to a boundary. *Biophys. J.* **89** (6), 3771–3779.

HANCOCK, G. J. 1953 The self-propulsion of microscopic organisms through liquids. *Proc. R. Soc. Lond.* A **217** (1128), 96–121.

HIGDON, J. J. L. 1979 The hydrodynamics of flagellar propulsion: helical waves. *J. Fluid Mech.* **94** (2), 331–351.

HOMMA, M., OOTA, H., KOJIMA, S., KAWAGISHI, I. & IMAE, Y. 1996 Chemotactic responses to an attractant and a repellent by the polar and lateral flagellar systems of *Vibrio alginolyticus*. *Microbiology* **142**, 2777–2783.

https://doi.org/10.1017/jfm.2018.799 Published online by Cambridge University Press

HSU, C. & DILLON, R. 2009 A 3D motile rod-shaped monotrichous bacterial model. *Bull. Math. Biol.* **71** (5), 1228–1263.

ISHIKAWA, T. 2009 Suspension biomechanics of swimming microbes. *J. R. Soc. Interface* **6** (39), 815–834.

ISHIKAWA, T., SEKIYA, G., IMAI, Y. & YAMAGUCHI, T. 2007 Hydrodynamic interactions between two swimming bacteria. *Biol. J.* **93** (6), 2217–2225.

KAWAGISHI, I., IMAGAWA, M., IMAE, Y., MCCARTER, L. & HOMMA, M. 1996 The sodium-driven polar flagellar motor of marine Vibrio as the mechanosensor that regulates lateral flagellar expression. *Mol. Microbiol.* **20** (4), 693–699.

KIM, M. J., BIRD, J. C., PARYS, A. J. V., BREUER, K. S. & POWERS, T. R. 2003 A macroscopic scale model of bacterial flagellar bundling. *Proc. Natl Acad. Sci. USA* **100** (26), 15481–15485.

KIM, Y. & PESKIN, C. S. 2007 Penalty immersed boundary method for an elastic boundary with mass. *Phys. Fluids* **19** (5), 053103.

KIM, Y. & PESKIN, C. S. 2016 A penalty immersed boundary method for a rigid body in fluids. *Phys. Fluids* **28** (3), 033603.

KO, W., LIM, S., LEE, W., KIM, Y., BERG, H. C. & PESKIN, C. S. 2017 Modeling polymorphic transformation of rotating bacterial flagella in a viscous fluid. *Phys. Rev.* E **95** (6), 063106.

KUDO, S., IMAI, N., NISHITOBA, M., SUGIYAMA, S. & MAGARIYAMA, Y. 2005 Asymmetric swimming pattern of *Vibrio alginolyticus* cells with single polar flagella. *FEMS Microbiol. Lett.* **242** (2), 221–225.

LAUGA, E. 2016 Bacterial hydrodynamics. *Annu. Rev. Fluid Mech.* **48**, 105–130.

LAUGA, E. & POWERS, T. R. 2009 The hydrodynamics of swimming microorganisms. *Rep. Prog. Phys.* **72** (9), 096601.

LEE, W., KIM, Y., OLSON, S. D. & LIM, S. 2014 Nonlinear dynamics of a rotating elastic rod in a viscous fluid. *Phys. Rev.* E **90** (3), 033012.

LEWIS, C. L., CRAIG, C. C. & SENECAL, A. G. 2014 Mass and density measurements of live and dead gram-negative and gram-positive bacterial populations. *Appl. Environ. Microbiol.* **80** (12), 3622–3631.

LIM, S., FERENT, A., WANG, X. S. & PESKIN, C. S. 2008 Dynamics of a closed rod with twist and bend in fluid. *SIAM J. Sci. Comput.* **31** (1), 273–302.

LIM, S. & PESKIN, C. S. 2012 Fluid-mechanical interaction of flexible bacterial flagella by the immersed boundary method. *Phys. Rev.* E **85**, 036307.

MAGARIYAMA, Y., MASUDA, S., TAKANO, Y., OHTANI, T. & KUDO, S. 2001 Difference between forward and backward swimming speeds of the single polar-flagellated bacterium, *Vibrio alginolyticus*. *FEMS Microbiol. Lett.* **205** (2), 343–347.

MCCARTER, L. L. 2001 Polar flagellar motility of the *Vibrionaceae*. *Microbiol. Mol. Biol. Rev.* **65** (3), 445–462.

OLSON, S., LIM, S. & CORTEZ, R. 2013 Modeling the dynamics of an elastic rod with intrinsic curvature and twist using a regularized Stokes formulation. *J. Comput. Phys.* **238**, 169–187.

PARK, Y., KIM, Y., KO, W. & LIM, S. 2017 Instabilities of a rotating helical rod in a viscous fluid. *Phys. Rev.* E **95** (2), 022410.

PHAN-THIEN, N., TRAN-CONG, T. & RAMIA, M. 1987 A boundary-element analysis of flagellar propulsion. *J. Fluid Mech.* **184**, 533–549.

PURCELL, E. M. 1997 The efficiency of propulsion by rotating flagellum. *Proc. Natl Acad. Sci. USA* **94** (21), 11307–11311.

RAMIA, M., TULLOCK, K. L. & PHAN-THIEN, N. 1993 The role of hydrodynamic interaction in the locomotion of microorganisms. *Biophys. J.* **65** (2), 755–778.

RODENBORN, B., CHEN, C., SWINNEY, H. L., LIU, B. & ZHANG, H. P. 2013 Propulsion of microorganisms by helical flagellum. *Proc. Natl Acad. Sci. USA* **110** (5), 338–347.

SEN, A., NANDY, R. K. & GHOSH, A. N. 2004 Elasticity of flagellar hooks. *J. Electron Microsc.* **53** (3), 305–309.

SHUM, H. & GAFFNEY, E. A. 2012 The effects of flagellar hook compliance on motility of monotrichous bacteria: a modeling study. *Phys. Fluids* **24** (6), 061901.

https://doi.org/10.1017/jfm.2018.799 Published online by Cambridge University Press

SHUM, H., GAFFNEY, E. A. & SMITH, D. J. 2010 Modelling bacterial behaviour close to a no-slip plane boundary: the influence of bacterial geometry. *Proc. R. Soc. Lond.* A **466**, 1725–1748.

SON, K., GUASTO, J. S. & STOCHER, R. 2013 Bacteria can exploit a flagellar buckling instability to change direction. *Nat. Phys.* **9**, 494–498.

STOCKER, R. 2011 Reverse and flick: hybrid locomotion in bacteria. *Proc. Natl Acad. Sci. USA* **108** (7), 2635–2636.

TAKANO, Y., YOSHIDA, K., KUDO, S., NISHITOBA, M. & MAGARIYAMA, Y. 2003 Analysis of small deformation of helical flagellum of swimming *Vibrio alginolyticus*. *JSME. Intl J.* **46** (4), 1241–1247.

TAYLOR, G. I. 1952 The action of waving cylindrical tails in propelling microscopic organisms. *Proc. R. Soc. Lond.* A **211** (1105), 225–239.

THAWANI, A. & TIRUMKUDULU, M. S. 2017 Trajectory of a model bacterium. *J. Fluid Mech.* **835**, 252–270.

TIMOSHENKO, S. 1961 *Theory of Elastic Stability*, 2nd edn. McGraw-Hill.

WENG, Y., DELGADO, F. F., SON, S., BURG, T. P., WASSERMAN, S. C. & MANALIS, S. R. 2011 Mass sensors with mechanical traps for weighing single cells in different fluids. *Lab on a Chip* **11**, 4174–4180.

XIE, L., ALTINDAL, T., CHATTOPADHYAY, S. & WU, X. L. 2010 Bacterial flagellum as a propeller and as a rudder for efficient chemotaxis. *Proc. R. Soc. Lond.* A **108** (6), 2246–2251.

https://doi.org/10.1017/jfm.2018.799 Published online by Cambridge University Press